Real-time pressure estimation on wings in unsteady conditions 122114

Pierangelo Masarati
POLITECNICO DI MILANO

09/07/2016
Final Report

Air Force Research Laboratory
AF Office Of Scientific Research (AFOSR)/ IOE
Arlington, Virginia 22203
Air Force Materiel Command

REPORT DOCUMENTATION PAGE

Form Approved
OMB No. 0704-0188

The public reporting burden for this collection of information is estimated to average 1 hour per response, including the time for reviewing instructions, searching existing data sources, gathering and maintaining the data needed, and completing and reviewing the collection of information. Send comments regarding this burden estimate or any other aspect of this collection of information, including suggestions for reducing the burden, to Department of Defense, Executive Services, Directorate (0704-0188). Respondents should be aware that notwithstanding any other provision of law, no person shall be subject to any penalty for failing to comply with a collection of information if it does not display a currently valid OMB control number.
PLEASE DO NOT RETURN YOUR FORM TO THE ABOVE ORGANIZATION.

1. REPORT DATE *(DD-MM-YYYY)*	2. REPORT TYPE	3. DATES COVERED *(From - To)*
07-09-2016	Final	15 Aug 2012 to 14 Feb 2016

4. TITLE AND SUBTITLE
Real-time wing-vortex and pressure distribution estimation on wings via displacement and strains in unsteady and transitional flight conditions

5a. CONTRACT NUMBER

5b. GRANT NUMBER
FA8655-12-1-2114

5c. PROGRAM ELEMENT NUMBER
61102F

6. AUTHOR(S)
Pierangelo Masarati

5d. PROJECT NUMBER

5e. TASK NUMBER

5f. WORK UNIT NUMBER

7. PERFORMING ORGANIZATION NAME(S) AND ADDRESS(ES)
POLITECNICO DI MILANO
PIAZZA LEONARDO DA VINCI 32
MILANO, 20133 IT

8. PERFORMING ORGANIZATION REPORT NUMBER

9. SPONSORING/MONITORING AGENCY NAME(S) AND ADDRESS(ES)
EOARD
Unit 4515
APO AE 09421-4515

10. SPONSOR/MONITOR'S ACRONYM(S)
AFRL/AFOSR IOE

11. SPONSOR/MONITOR'S REPORT NUMBER(S)
AFRL-AFOSR-UK-TR-2016-0019

12. DISTRIBUTION/AVAILABILITY STATEMENT
A DISTRIBUTION UNLIMITED: PB Public Release

13. SUPPLEMENTARY NOTES

14. ABSTRACT
The analysis of thin structural components, which are characteristic of a broad class of Micro Air Vehicles, is presented herein. A direct solution approach in co simulation with fluid-dynamics solvers is used. An original variational formulation is developed for the inverse problem of reconstructing full-field structural displacement and pressure distribution of membrane wings subjected to static and unsteady loads from membrane strain distribution. Moving Least Squares are used to smooth and remap surface strain measurements, estimated from Digital Image Correlation (DIC), as needed by the inverse solution meshing. The same approach is used to map the structural and fluid interface kinematics and loads during the fluid structure co-simulation. The inverse analysis is verified by reconstructing the deformed solution obtained with a corresponding direct formulation, based on nonlinear membrane structural analysis implemented in a free general-purpose multibody dynamics solver and tightly coupled in co-simulation with a CFD solver. Both the direct and the inverse analyses are validated by comparing the direct predictions and the reconstructed deformations with experimental data for prestressed rectangular membranes subjected to static and unsteady loads. The load distributions reconstructed using the inverse analysis are compared with the corresponding ones obtained using the direct analysis. The inverse analysis runs on standard off the-shelf PCs and can be implemented in real-time, providing load distribution estimates at a rate in the order of tens of datasets per second.

15. SUBJECT TERMS
MAV, membrane wing, EOARD

16. SECURITY CLASSIFICATION OF:			17. LIMITATION OF ABSTRACT	18. NUMBER OF PAGES	19a. NAME OF RESPONSIBLE PERSON
a. REPORT	b. ABSTRACT	c. THIS PAGE			CUMMINGS, RUSSELL
Unclassified	Unclassified	Unclassified	SAR	40	19b. TELEPHONE NUMBER *(Include area code)* 011-44-1895-616021

Standard Form 298 (Rev. 8/98)
Prescribed by ANSI Std. Z39.18

Real-Time Wing-Vortex And Pressure Distribution Estimation on Wings Via Displacements and Strains in Unsteady and Transitional Flight Conditions

Mattia Alioli[1], Pierangelo Masarati[2], Marco Morandini[3]
Politecnico di Milano, Milano, 20156, Italy

Trenton Carpenter[4], N. Brent Osterberg[5] Roberto Albertani[6]
Oregon State University, Corvallis, Oregon, 97330, USA

February 14, 2016

[1]Research Assistant, Dipartimento di Scienze e Tecnologie Aerospaziali, via La Masa 34, 20156 Milano, mattia.alioli@polimi.it

[2]Associate Professor, Dipartimento di Scienze e Tecnologie Aerospaziali, via La Masa 34, 20156 Milano, pierangelo.masarati@polimi.it

[3]Associate Professor, Dipartimento di Scienze e Tecnologie Aerospaziali, via La Masa 34, 20156 Milano, marco.morandini@polimi.it

[4]Research Assistant, Mechanical Engineering, 204 Rogers Hall Corvallis OR 97330, trenton.carpenter@gmail.com

[5]Research Assistant, Mechanical Engineering, 204 Rogers Hall Corvallis OR 97330, osterben@onid.oregonstate.edu

[6]Associate Professor, Mechanical Engineering, 204 Rogers Hall Corvallis OR 07330, roberto.albertani@oregonstate.edu

Abstract

The analysis of thin structural components, which are characteristic of a broad class of Micro Air Vehicles, is presented herein. A direct solution approach in co-simulation with fluid-dynamics solvers is used. An original variational formulation is developed for the inverse problem of reconstructing full-field structural displacement and pressure distribution of membrane wings subjected to static and unsteady loads from membrane strain distribution. Moving Least Squares are used to smooth and remap surface strain measurements, estimated from Digital Image Correlation (DIC), as needed by the inverse solution meshing. The same approach is used to map the structural and fluid interface kinematics and loads during the fluid-structure co-simulation. The inverse analysis is verified by reconstructing the deformed solution obtained with a corresponding direct formulation, based on nonlinear membrane structural analysis implemented in a free general-purpose multibody dynamics solver and tightly coupled in co-simulation with a CFD solver. Both the direct and the inverse analyses are validated by comparing the direct predictions and the reconstructed deformations with experimental data for prestressed rectangular membranes subjected to static and unsteady loads. The load distributions reconstructed using the inverse analysis are compared with the corresponding ones obtained using the direct analysis. The inverse analysis runs on standard off-the-shelf PCs and can be implemented in real-time, providing load distribution estimates at a rate in the order of tens of datasets per second.

Contents

DISTRIBUTION A. Approved for public release: distribution unlimited.

Chapter 1

Formulation

1.1 Introduction

The work presented within this paper seeks to obtain full-field estimations of the structural displacement field for a membrane wing for Micro Air Vehicle (MAV) applications. The source of these estimations is the elastic wing deformation, experimentally measured in a low-speed wind tunnel using a full-field, non-contact, digital image correlation (DIC) technique, originally developed by researchers at the University of South Carolina [30].

MAVs were defined by the Defense Advanced Research Projects Agency as aircraft with wingspan less than 15 cm and a maximum speed less than 15 m/s. These aircraft can be utilized for a variety of missions, carrying payload such as surveying and sensing equipment. In MAV designs, much like natural fliers, compliant membranes are used to passively enhance flight characteristics. Membrane wings display unique aerodynamic characteristics due to their aeroelastic nature, which can provide performance improvements over their rigid airfoil counterparts. Extensive research has been conducted on the dynamics of flexible wings, but limited research exists on practical, computationally predictive models dealing with the dynamic behavior surrounding these wings.

Stanford et al. [28] analyzed the effect of a flexible membrane on a fixed wing with both experiments and numerical modeling. They modeled the membrane as inextensible, using a linear stress-stiffening model. The linear stress-strain assumption held well, because the strain accumulated due to the aerodynamic load was small in comparison with the prestrain of the membrane. Utilizing experimentally measured deformations of a membrane wing in a wind tunnel they successfully predicted the aerodynamic forces over the wing for a range of flight speeds and angles of attack: an inverse technique was formulated by locating a pressure field that minimizes the least-squares difference between experimental displacements and calculated values; the calculated pressure field was then used to qualitatively describe the important flow characteristic over the membrane wing, including flow stagnation, pressure recovery, flow reattachment and wing tip vortices.

Because of unsteadiness, flow separation, and turbulence, previous studies using panel methods and simplified laminar solvers have failed to capture the exact effect of membrane wings on performance. Gopalakrishnan and Tafti [15] addressed this issue by analyzing flapping flight for a flexible wing (at low Reynolds number) using an unsteady large-eddy simulation (LES) flow solver coupled with a linear elastic membrane wing model. The focus of the study was to evaluate the effect of aeroelastic cambering on flapping flight performance using a linear elastic membrane model with different prestress values. The wing is treated as an elastic membrane with in-plane prestresses. The prestresses of the wing are tailored to induce a camber in the range of 0.1-0.25 times the chord length, and their effect is analyzed based on changes in flow structure and on variation of thrust and lift. They showed that the introduction of camber increases thrust and lift production significantly, although the transverse displacement was up to 25% of the chord, which means a membrane strain of more than 12%, which in turn may cause substantial change of the membrane stress, making the problem strongly nonlinear. In practice, the linearized structural

model, which assumes constant membrane prestress, is inadequate for straining of such magnitude.

Inverse FEM analysis has been proposed also to identify the mechanical properties of membranes, e.g. when for nontraditional methods are needed for characterizing the behavior of materials when the associated boundary problems is complex [18, 17]. These methods finds several applications for example in the identification of the mechanical properties of biological tissues [1].

The present work discusses a variational principle that provides the mathematical framework from which a robust inverse finite element method (IFEM) is developed. The problem at hand is the reconstruction of the three-dimensional deformations of membrane structures based upon the experimentally measured (discrete) surface strains (and well-defined boundary restraints), experienced by a flexible wing during flight, and the estimation of the aerodynamic pressure exerted on the wing. With an estimate of the pressure distribution, aerodynamic loads can be estimated, as attempted for example in Carpenter and Albertani [10]. The actual loads that cause the deformations are unknown; however, their influences are represented in the measured strains. This "inverse" technique (as opposed to a conventional "direct" technique: estimating the displacement field from a measured pressure distribution) represents a viable alternative to conventional pressure measurement techniques in low Reynolds number environments. In fact, the thin elastic membrane wing skins used to decrease the vehicle weight and obtain a certain amount of passive shape adaptation [26] are particularly susceptible to intrusive measurements.

Currently, the numerical validation of the flow field created by a MAV wing is largely limited to (i) a comparison of numerical aerodynamic coefficients with those garnered through wind tunnel test analysis [29], or (ii) a comparison with flow visualization, focusing on the flow separation, transition, and reattachment locations over the wing [20]. Knowledge of the full-field differential pressure distribution over the wing surface can provide a further level of comparison, indicating areas over the wing where the model may be inadequate. An inverse method could take the deformed wing shapes and estimate the resulting pressure distribution within flight regimes that are difficult, if not impossible to simulate through either CFD or wind tunnel testing.

Aerodynamically, inverse problems have two main applications: they could be used for inverse design problems for optimal airfoil geometries [14], or for structural health monitoring (an elastic wing is mounted with deformation sensors, typically strain gages or fiber-optics, whose signals are used to reconstruct the displacement field [31], or the original wing loading [25]).

1.2 Methodology

A membrane structural model is developed for both direct and inverse dynamics. The direct dynamics analysis is used to predict the deformed shape under specified loads. The inverse kinematics analysis is used to reconstruct the membrane shape from the membrane strain field. The inverse dynamics analysis is used to reconstruct the pressure distribution.

A membrane finite element, implemented in a multibody formulation [22], is used in co-simulation with a fluid dynamics solver to predict the configuration of the system under static and unsteady loads [2, 3].

An original approach is developed for the inverse problem of the reconstruction of full-field structural displacements of membrane wings utilizing surface strain measurements [4, 6].

The inverse problem of full-field structural displacement reconstruction is addressed through the application of a variational formulation, leading to a versatile, robust and computationally efficient inverse membrane nonlinear finite element analysis [5], which was inspired by analogous, although linear, approaches developed in the past for shell-like structures, see Shkarayev et al. [25], Tessler and Spangler [31].

In the current case, nonlinear elasticity is mandatory to capture the essence of the transverse load carrying capability of membranes, whereas in the previous mentioned prior formulations the problem was restricted to linear elasticity: when subjected to a finite amount of transverse displacement, the assumption of constant membrane prestress used in linearized membrane models is no longer acceptable. The complete set of membrane strain measures, consistent with non-linear membrane theory, need to be used.

Exploiting the functionalities provided by the free software project FEniCS[1] (a collection of libraries specifically designed for the automated and efficient solution of PDEs), a three-node inverse membrane element was developed (see Alioli et al. [4]): three displacement degrees of freedom are used for each node, namely two displacement components in the plane of the membrane and one along the transverse direction. The error function is the difference between the membrane strain measures expressed as functions of the displacements and the corresponding membrane strain measures obtained from the experimental strains by re-sampling.

A penalty-parameter controlled regularization term mitigates the ill-posedness of the problem associated with the non-uniqueness of the solution in terms of transverse displacement for given membrane stresses and with the high-order nonlinearity of the membrane strains with respect to transverse displacement. In fact, in addition to the usual level of ill-posedness of linear inverse problems (they do not necessarily satisfy conditions of existence, uniqueness, and stability, see for example Bakushinsky and Goncharsky [9], Shkarayev et al. [25]), the present one is also characterized by the fact that for null or low membrane prestress the problem is exactly singular in configurations that present no transverse displacement of the membrane.

The reconstructed shape of the membrane is used to estimate the surface loads. The procedure is verified and validated by correlation with the surface load values predicted by the coupled fluid-structure analysis.

The present work uses an experimental setup that can accurately obtain the full-field three-dimensional displacement and membrane strain over a moderate size wing in wind tunnel testing conditions. The proposed methodology enables accurate reconstruction of the three-dimensional displacement field. It may be effectively employed to develop real-time processing of the sensed information.

Analytical and numerical results, along with experimental measurements of actual membrane wing artifacts subjected to a variety of steady and unsteady flow conditions are used to validate the proposed formulation.

Experimental data is based on DIC in conjunction with a load cell and tensile test frame to measure stress and strains: DIC measurements were taken to generate virtual strain sensors on the surface of the membrane [10]. Measurements are further manipulated using moving least-squares (MLS) [24] to remap the measured displacements and strains on the same grid that is used for the inverse analysis.

Historically, due to its commercial availability, the membrane used in the experiments has been made of isotropic material. Methods such as pretension before mounting it on a frame have been developed to alter its characteristics. However, by developing a non-isotropic elastic membrane material capable of being tailored to an applicable stiffness range for membrane-based wings, researchers might be able to better replicate the successful characteristics of natural fliers. A non-isotropic membrane, in fact, should response differently to pressure loading between the longitudinal and transverse direction: this response could be used to vary designed flight characteristics of future membrane wings [32]. Thus, a hydrostatic membrane pressure test was also conducted to characterize the behavior of the non-isotropic membrane under a constant and uniform pressure distribution. A non-isotropic and a silicone control sample were each secured over a frame and subjected to a pressure differential across the membrane. The membrane response to the pressure differential is used to predict the membrane behavior under aerodynamic loading. As researchers refine membrane wing designs, the availability of elastic, non-isotropic material similar to bat wings will provide another tool in the development of a functional MAV membrane design with potential for expanding their flight envelope.

1.3   Origin of Least-Squares Problems

In this section, the basics of the Least-Squares problem are recalled, to provide the essential background for the formulation of the inverse problem that is developed in Section 1.4.

---

[1] http://fenicsproject.org/

A variety of practical problems can be formulated as the minimization of the square of an error function; i.e., of a scalar function $F(\mathbf{x})$ which can be expressed as a sum of squares of nonlinear functions:

$$F(\mathbf{x}) = \frac{1}{2} \sum_{i=1}^{m} f_i(\mathbf{x})^2 = \frac{1}{2} \|\mathbf{f}(\mathbf{x})\|^2 \tag{1.1}$$

where $\mathbf{x} = (x_1, x_2, \ldots, x_n)$ is a vector and each f_i is a function from $\mathbb{R}^n$ to $\mathbb{R}$. The factor $\frac{1}{2}$ has been included in (1.1) in order to avoid the appearance of a factor 2 in the derivatives. The f_i are referred to as residuals. It is assumed that $m \geq n$.

Although function (1.1) can be minimized by a variety of unconstrained methods, in most circumstance the properties of (1.1) make it worthwhile to use methods designed specifically for the least-squares problem. In particular, the gradient and Hessian of (1.1) have a special structure. Let the $m \times n$ Jacobian matrix of $\mathbf{f}(\mathbf{x})$ be denoted by $\mathbf{J}(\mathbf{x})$, and let matrix $\mathbf{G}_i(\mathbf{x})$ denote the Hessian matrix of $f_i(\mathbf{x})$. Then

$$\mathbf{g}(\mathbf{x}) = \mathbf{J}(\mathbf{x})^T \mathbf{f}(\mathbf{x}) \tag{1.2}$$

$$\mathbf{G}(\mathbf{x}) = \mathbf{J}(\mathbf{x})^T \mathbf{J}(\mathbf{x}) + \mathbf{Q}(\mathbf{x}) \tag{1.3}$$

where $\mathbf{Q}(\mathbf{x}) = \sum_{i=1}^{m} f_i(\mathbf{x}) \mathbf{G}_i(\mathbf{x})$. From (1.3) we can observe that the Hessian of a least-squares objective function consists of a special combination of first- and second-order information. Typically, least-squares methods are based on the hypothesis that eventually the first-order term $\mathbf{J}(\mathbf{x})^T \mathbf{J}(\mathbf{x})$ of (1.3) becomes dominant with respect to the second-order term $\mathbf{Q}(\mathbf{x})$. This assumption is not justified when the residuals at the solution are very large: in such a case, one might as well use a general unconstrained method. However, for many problems, the residual at the solution is small enough to justify the use of a special method.

1.3.1   The Gauss-Newton Method

Vanilla gradient descent is the simplest and most intuitive technique to find minima in a function, but it suffers from various convergence problems. This situation can be improved upon by using curvature as well as gradient information, namely second derivatives. One way to do this is to use Newton's method to solve the equation $\mathbf{g}(\mathbf{x}) = \mathbf{J}(\mathbf{x})^T \mathbf{f}(\mathbf{x}) = \mathbf{0}$.

From (1.3), the Newton equation becomes $\mathbf{G}_k \mathbf{p}_k = -\mathbf{g}_k$, or:

$$(\mathbf{J}_k^T \mathbf{J}_k + \mathbf{Q}_k) \mathbf{p}_k = -\mathbf{J}_k^T \mathbf{f}_k \tag{1.4}$$

where a quantity subscribed by k denotes that quantity evaluated at $\mathbf{x}_k$, the current estimate of the solution. Let $\mathbf{p}_N$ denote the solution of (1.4), i.e., the Newton direction.

If $\|\mathbf{f}_k\|$ tends to zero as $\mathbf{x}_k$ approaches the solution, matrix $\mathbf{Q}_k$ also tends to zero, so equation (1.4) can be approximated by the following equation, which involves only the first derivatives of $\mathbf{f}$:

$$\mathbf{J}_k^T \mathbf{J}_k \mathbf{p}_k = -\mathbf{J}_k^T \mathbf{f}_k \tag{1.5}$$

The solution of (1.5) is a solution of the linear least-squares problem

$$\underset{\mathbf{p} \in \mathbb{R}^n}{\text{minimize}} \; \frac{1}{2} \|\mathbf{J}_k \mathbf{p} + \mathbf{f}_k\|_2^2 \tag{1.6}$$

and is unique if $\mathbf{J}_k$ has full column rank. The vector $\mathbf{p}_{GN}$ that solves (1.6) is called Gauss-Newton direction, and the method in which this vector is used as a search direction is known as the Gauss-Newton method. Early implementations of the Gauss-Newton method typically formed the explicit matrix $\mathbf{J}_k^T \mathbf{J}_k$ and computed $\mathbf{p}_{GN}$ by solving equation (1.5). The disadvantage of this approach is that the condition number of $\mathbf{J}_k^T \mathbf{J}_k$ is the square of that of $\mathbf{J}_k$. Consequently, unnecessary error may occur in determining the search direction.

Ill-conditioning is a common feature of nonlinear least-squares problems derived from parameter estimation problems, because the underlying mathematical model is often ill-defined. Unnecessary worsening of the conditioning can be avoided by solving the linear least-squares problem (1.6) using the complete orthogonal factorization or the singular-value decomposition.

In the rank-deficient case, any implementation that uses a minimum-norm solution to (1.6) must include a strategy for estimating the rank of $\mathbf{J}_k$.

1.3.2 The Levenberg-Marquardt Method

It can be seen that simple gradient descent and Gauss-Newton iteration are complementary in the advantages they provide. Levenberg [19] proposed an algorithm based on this observation, whose update rule is a blend of the above mentioned algorithms.

The Levenberg search direction is defined as the solution of the equations

$$(\mathbf{J}_k^T \mathbf{J}_k + \lambda_k \mathbf{I})\mathbf{p}_k = -\mathbf{J}_k^T \mathbf{f}_k \tag{1.7}$$

where λ_k is a non-negative scalar.

If the error reduces following an update, it implies that the quadratic assumption on $F(\mathbf{x})$ is working and the scalar λ_k con be reduced (usually by a factor of 10) to reduce the influence of gradient descent. On the other hand, if the error goes up, it is necessary to follow the gradient more; thus, λ_k is increased by the same factor.

The above algorithm has the disadvantage that if the value of λ_k is large, the calculated Hessian matrix is not used at all. We can derive some advantage out of the second derivative even in such cases by scaling each component of the gradient according to the curvature. This should result in larger movement along the directions where the gradient is smaller. This crucial insight was provide by Marquardt [21]. He replaced the identity matrix in (1.7) with the diagonal of the Hessian resulting in the Levenberg-Marquardt update rule

$$(\mathbf{J}_k^T \mathbf{J}_k + \lambda_k \operatorname{diag}(\mathbf{G}_k))\mathbf{p}_k = -\mathbf{J}_k^T \mathbf{f}_k \tag{1.8}$$

Since the Hessian is proportional to the curvature of $F(\mathbf{x})$, (1.8) implies a large step in the direction with low curvature and a small step in the direction with high curvature.

It is to be noted that while the LM method is in no way optimal but is just a heuristic, it works extremely well in practice. The only flaw is its need for matrix inversion as part of the update. Even though the inverse is usually implemented using clever pseudo-inverse methods such as singular value decomposition, the cost of the update becomes prohibitive after the model size increases to a few thousand parameters. For moderately sized models (of a few hundred parameters) however, this method is much faster than say, vanilla gradient descent.

Historically, the LM algorithm was presented by Marquardt as given above, where the parameter, λ, was manipulated directly to find the minimum. Subsequently, a trust-region approach to the algorithm has gained ground. The idea of the model trust-region approach is to accept the minimum of the quadratic model only as long as the quadratic model adequately reflects the behavior of F. Usually, the decision as to whether the model is acceptable is based on the norm of the computed search direction.

A unit step is always taken along $\mathbf{p}_k$ in (1.7), i.e., $\mathbf{x}_{k+1}$ is given by $\mathbf{x}_k + \mathbf{p}_k$, where $\mathbf{p}_k$ is the solution of the constrained subproblem

$$\underset{\mathbf{p} \in \mathbb{R}^n}{\text{minimize}} \quad \frac{1}{2} \|\mathbf{J}_k \mathbf{p} + \mathbf{f}_k\|_2^2 \tag{1.9}$$

$$\text{subject to} \quad \|\mathbf{p}\|_2 \leq \Delta \tag{1.10}$$

for some $\Delta > 0$. It can be shown that the solution of the equations (1.7) solves the subproblem (1.9) if either $\lambda = 0$ and $\|\mathbf{p}\|_2 \leq \Delta$, or $\lambda \geq 0$ and $\|\mathbf{p}\|_2 = \Delta$.

Thus, if Δ is large enough, the solution of (1.9) is simply the Newton direction (i.e., the solution of (1.7) with $\lambda = 0$). Otherwise, the restriction on the norm will apply, and $\|\mathbf{p}\|_2 = \Delta$. The search direction is typically found by solving (1.9) for trial values of Δ and evaluating F at the resulting trial points. A vector $\mathbf{p}$ such that $F(\mathbf{x}_k + \mathbf{p})$ is sufficiently less than F_k must exists for small enough Δ since the second-order term of the model function may be made small compared to the first-order term. As $\Delta \to 0$, $\|\mathbf{p}\|_2 \to 0$ and $\mathbf{p}$ becomes parallel to the steepest-descent direction.

1.4 Membrane Inverse Analysis

A membrane is a thin structural element, i.e., an element whose size in one direction (the thickness, z or 3 in the following) is extremely small compared with the other two (x and y or 1 and 2 in
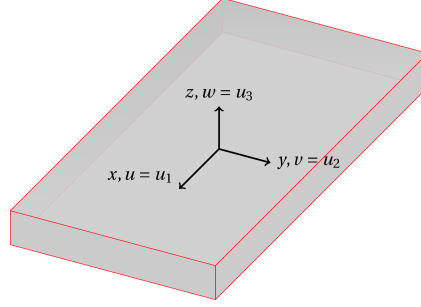
Figure 1.1: Membrane model.

the following), see Figure 1.1. The transverse gradients of strain and stress components along the reference surface of the membrane are negligible. As a consequence, a membrane cannot withstand transverse loads unless some in-plane prestress is present.

1.4.1 Kinematics

Assuming, from the point of view of kinematics, that in-plane strains are uniform throughout the thickness of the membrane, strain measurements on just one side of the membrane would be sufficient to characterize the in-plane strain field (on the contrary, in the case of a shell, the average of the measurements on both surfaces would be needed to eliminate the effect of bending).

The membrane strains, i.e., the in-plane components of the Green-Lagrange strain tensor, defined as:

$$\varepsilon_x = u_{/x} + \frac{1}{2}\left(u_{/x}^2 + v_{/x}^2 + w_{/x}^2\right) \tag{1.11a}$$

$$\varepsilon_y = v_{/y} + \frac{1}{2}\left(u_{/y}^2 + v_{/y}^2 + w_{/y}^2\right) \tag{1.11b}$$

$$\gamma_{xy} = u_{/y} + v_{/x} + u_{/x}u_{/y} + v_{/x}v_{/y} + w_{/x}w_{/y}, \tag{1.11c}$$

can be collected in a vector $\boldsymbol{\varepsilon}$:

$$\boldsymbol{\varepsilon} = \left\{ \begin{array}{c} \varepsilon_x \\ \varepsilon_y \\ \gamma_{xy} \end{array} \right\} = \left\{ \begin{array}{c} \varepsilon_{11} \\ \varepsilon_{22} \\ 2\varepsilon_{12} \end{array} \right\} \tag{1.12}$$

or

$$\varepsilon_{ij} = \frac{1}{2}\left(u_{i/j} + u_{j/i} + \mathbf{u}_{/i}^T\mathbf{u}_{/j}\right) \tag{1.13}$$

where $(\clubsuit)_{/(\spadesuit)}$ indicates the derivative of $(\clubsuit)$ with respect to $(\spadesuit)$, vector $\mathbf{u} = \{u; v; w\} = \{u_1; u_2; u_3\}$ collects the displacement components in the plane of the membrane, $u = u_1$ and $v = u_2$ and the one along the transverse direction, $w = u_3$.

1.4.2 Cost Function

The inverse kinematics problem can be formulated by defining an appropriate cost function of the error $\mathbf{e}$ between the measured and the configuration-dependent strains.

Consider a set of strain measurements $\varepsilon_x^{(m)}$, $\varepsilon_y^{(m)}$, and $\gamma_{xy}^{(m)}$, e.g. DIC, namely:

$$\boldsymbol{\varepsilon}^{(m)} = \left\{ \begin{array}{c} \varepsilon_x^{(m)} \\ \varepsilon_y^{(m)} \\ \gamma_{xy}^{(m)} \end{array} \right\}, \tag{1.14}$$

that correspond to the configuration-dependent strains defined earlier.

The error $\mathbf{e}$ is

$$\mathbf{e} = \boldsymbol{\varepsilon}(\mathrm{Grad}(\mathbf{u})) - \boldsymbol{\varepsilon}^{(\mathrm{m})}, \tag{1.15}$$

with $\mathrm{Grad}(\clubsuit) = \{(\clubsuit)_{/x}; (\clubsuit)_{/y}\}$.

The following cost function is considered:

$$\Phi(\mathbf{u}) = \Phi_{\mathbf{e}}(\mathbf{u}) + k\Phi_{\mathbf{u}} \tag{1.16}$$

where:

- $\Phi_{\mathbf{e}}(\mathbf{u})$ is a quadratic function of the error $\mathbf{e}$,

$$\Phi_{\mathbf{e}}(\mathrm{Grad}(\mathbf{u})) = \frac{1}{2}\int_A \mathbf{e}^T \mathbf{D}\mathbf{e} \ \mathrm{d}A \tag{1.17}$$

with $\mathbf{D}$ an arbitrary positive definite weighting matrix; e.g., but not necessarily, the plane stress constitutive properties matrix, which for isotropic materials is

$$\mathbf{D} = \frac{E}{1-\nu^2}\begin{bmatrix} 1 & \nu & 0 \\ \nu & 1 & 0 \\ 0 & 0 & (1-\nu)/2 \end{bmatrix} \tag{1.18}$$

- $\Phi_{\mathbf{u}}$ is a regularization contribution in the derivatives of w,

$$\Phi_{\mathbf{u}}(\mathbf{u}) = \frac{1}{2}\int_A (\mathrm{Grad}(w) - \mathrm{Grad}(w_{\mathrm{ref}}))^T \mathbf{T}(\mathrm{Grad}(w) - \mathrm{Grad}(w_{\mathrm{ref}})) \ \mathrm{d}A \tag{1.19}$$

with w_{ref} a reference transverse displacement, defined in Section 1.4.3, and the weighting matrix

$$\mathbf{T} = \begin{bmatrix} T_x & T_{xy} \\ T_{xy} & T_y \end{bmatrix} \tag{1.20}$$

defined in analogy with the strain energy contribution associated with pretension: $T_x > 0$, $T_y > 0$, and $\sqrt{T_x T_y} > |T_{xy}| \geq 0$ such that $\mathbf{T} > 0$ (positive definite);

- k is a parameter that restores dimensional consistency and weighs the regularization contribution.

1.4.3 Regularization

The regularization contribution is defined in such a manner that it naturally vanishes at convergence, by properly crafting the reference displacement, w_{ref}. Such correction is needed to add a positive definite quadratic contribution to the cost function, and thus make it convex on the entire domain. In fact, the minimization of $\Phi_{\mathbf{e}}(\mathbf{u})$ with respect to the actual displacement field $\mathbf{u}$ requires its partial derivatives with respect to each of the components u, v, and w to vanish. Clearly, as a consequence of the strain definitions of Eq. 1.11, $\Phi_{\mathbf{e}}(\mathrm{Grad}(\mathbf{u}))$ is not a convex function of w when $\mathrm{Grad}(w) \equiv \mathbf{0}$, i.e., when the membrane is parallel to the reference plane, and the problem is ill-posed in the vicinity of such condition.

This approach resembles the so-called damped least squares, also known as the Levenberg-Marquardt algorithm [19, 21], summarized in Section 1.3.2.

The inverse formulation does not need elastic or inertial material properties. The reference transverse displacement $w_{\mathrm{ref}} \neq 0$ is needed to deflect the solution towards a specific direction, since the same membrane strain pattern is obtained with $\pm w$. As suggested in Alioli et al. [4], one should choose a tentative initial value for w_{ref}: a convenient choice can be the one corresponding to a uniform pressure difference applied on the membrane, or in any case a prescribed displacement that qualitatively resembles the expected solution. Subsequently, the reference solution is updated by interpolating between the current value $w_{\mathrm{ref}}^{(i)}$ and the solution at the current step i, i.e., $w^{(i)} + \Delta w^{(i)}$, such that at convergence, when $\Delta w^{(i)} \cong 0$, then $(\mathrm{Grad}(w) - \mathrm{Grad}(w_{\mathrm{ref}})) \cong 0$. Thus, $w_{\mathrm{ref}}^{(i+1)} = (1-\alpha)w_{\mathrm{ref}}^{(i)} + \alpha(w^{(i)} + \Delta w^{(i)})$, where $0 < \alpha \leq 1$ is a relaxation parameter ($\alpha = 1$ implies no relaxation).
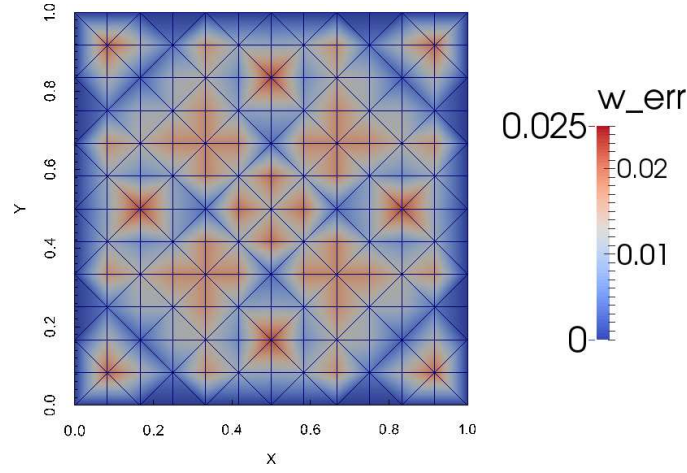
Figure 1.2: Deformation error of a square membrane subjected to uniform pressure.

1.4.4 Pressure Field Reconstruction

Finally, the estimated displacement field $\mathbf{u} = \{u; v; w\} = \{u_1; u_2; u_3\}$ can be used to estimate the distributed force field $\mathbf{p}$ acting on the membrane [6]:

$$\int_A \delta\boldsymbol{\varepsilon} : \boldsymbol{\sigma} \ \mathrm{d}A = \int_A \mathbf{p} \cdot \delta\mathbf{v} \ \mathrm{d}A \tag{1.21}$$

where $\boldsymbol{\sigma} = \boldsymbol{\sigma}(\boldsymbol{\varepsilon})$ is the known stress tensor, expressed as a function of the reconstructed strain tensor $\boldsymbol{\varepsilon} = \boldsymbol{\varepsilon}(\mathbf{u})$, and $\delta\mathbf{v}$ is an appropriate vector *test function*, which is required to vanish on the boundary ∂A of A. Thus, the reconstructed distributed force field $\mathbf{p}$ is expected not to be accurate along the boundary of the membrane domain, due to the choice of the boundary conditions.

1.4.5 Verification

In this section, a simple direct ("forward") membrane problem is considered in order to demonstrate how the inverse formulation lead to the reconstruction of the displacement solution consistent with the measured strain data. The exact strains are computed from the direct problem and are used to represent the measured strain data.

Consider a direct (forward) problem of a rectangular membrane bent under the action of the distributed transverse loading (hydrostatic pressure). The proposed inverse finite element analysis formulation is verified in Alioli et al. [4, 5] performing a direct analysis, obtained with the same finite element model (an edge-clamped square membrane without prestrain and subjected to uniform pressure on one side), but with a finer mesh, whose results are re-sampled to provide the membrane strain values at the points required by the inverse analysis. The re-sampled transverse displacements are used to verify the quality of the inverse analysis. The numerical solution, obtained using a fine mesh (20×20 pairs of elements), has been re-sampled using a much coarser mesh (10×10). A third, intermediate mesh (12×12) has been used for the IFEM procedure.

Figure 1.2 shows the transverse displacement error, computed as $w_{\mathrm{err}} = |w^{(\mathrm{fem})} - w| / \max |w^{(\mathrm{fem})}|$, where $w^{(\mathrm{fem})}$ is the transverse displacement obtained by the reference finite element analysis, whereas w is the transverse displacement reconstructed via IFEM.

The estimated displacement field is subsequently used to estimate the pressure acting on the membrane: Table 1.1 compares the resultant (normal) force error obtained by using the FEM pressure distribution (which is calculated from the displacements of the reference FEM analysis) and the one obtained by using the pressure distribution computed from the displacements estimated via IFEM analysis, with respect to the resultant (normal) force obtained considering the ideal uniform pressure distribution, i.e. pressure times the membrane surface area. To compute

the resultant forces, the near-boundary region was omitted from calculation, for the motivation just mentioned above.

Reference FEM solution	1.64 %
Inverse FEM analysis	5.25 %

Table 1.1: Resultant normal force error (not considering the near-boundary region), comparison of FEM and IFEM analysis with respect to the nominal value.

The results, in terms of transverse displacement, are satisfactory. Furthermore, as shown in Alioli et al. [6], the IFEM and the FEM pressure distributions are quite similar on the entire domain, although both of them are not significantly flat. This is expected, due to the choice of the boundary conditions. Nevertheless, the average values of the pressure distributions calculated using the reconstructed displacements and those from the FEM analysis do seem to be accurate, as seen from the resultant force errors (Tab. 1.1).

A typical inverse solution like the ones presented above, e.g., with a 12×12 mesh and a residual norm tolerance of 10^{-5}, requires 5 to 8 iterations for each load step. Each iteration requires about 27.5 ms on an off-the-shelf PC (in the present case, an Intel Core i7-2620M with CPU at 2.70 GHz). The property of computational efficiency is of utmost importance since the long term objective is the real-time implementation of the procedure.

1.4.6 Problem Well-Posedness

As we shall see, the membrane inverse problem may be ill-posed, and can have multiple solutions.

The geometry of a two-dimensional surface is characterized by two symmetric tensors, called the first and second fundamental forms of a surface. See Do Carmo [13] for details.
Let $\mathbf{x}(\xi^\alpha)$, with $\alpha = \{1, 2\}$, be the parametric equations of the surface. Let also $\mathbf{g}_\alpha = \mathbf{x}{,_\alpha} = \frac{\partial \mathbf{x}}{\partial \xi^\alpha}$ and $\mathbf{g}^\alpha$ be the covariant and contravariant surface base vectors, respectively, defined in such a way that $\mathbf{g}_\alpha \cdot \mathbf{g}^\beta = \delta_\alpha^\beta$, the Kronecker delta, with $\alpha, \beta = \{1, 2\}$.

The first fundamental form $\mathbf{a}$ of the surface is nothing but its metric tensor, defined in such a way that $\mathbf{x}{,_\alpha} = \mathbf{a} \cdot \mathbf{g}_\alpha$. It can be computed as $\mathbf{a} = \mathbf{g}^\alpha \otimes \mathbf{g}_\alpha \cdot \mathbf{g}_\beta \otimes \mathbf{g}^\beta$. The second fundamental form $\mathbf{b}$ of the surface describes the rate of change of the surface normal $\mathbf{n}$, viz.: $\mathbf{n}{,_\alpha} = -\mathbf{b} \cdot \mathbf{g}_\alpha$.

The fundamental theorem of the theory of surfaces states that the first and second fundamental forms of a surface determine its shape up to its position in space (for a self-contained, and essentially elementary proof, see Ciarlet and Larsonneur [12]). Thus, this theorem guarantees that, by knowing both the first and the second fundamental form, the inverse problem of reconstructing the surface is well-posed.

The ill-posedness of the inverse problem comes from the fact that, by measuring only the membranal strain tensor $\boldsymbol{\varepsilon}$ one actually accounts only for the first fundamental form, and not for the second. As a matter of fact, the membrane strain tensor $\boldsymbol{\varepsilon}$, Eq. (1.12), is nothing but the difference between the metric tensor $\mathbf{a}'$ in the deformed configuration $\mathbf{x}' = \mathbf{x} + \mathbf{u}$, computed with respect to the reference configuration, and the metric tensor in the reference configuration $\mathbf{a}$, viz.: $\boldsymbol{\varepsilon} = \frac{1}{2}(\mathbf{a}' - \mathbf{a})$. The difference between the second fundamental form in deformed and reference configuration, i.e., $\mathbf{k} = \mathbf{b}' - \mathbf{b}$, is, instead, a suitable measure of the flexure strain of a thin shell. This means that the inverse problem would be well-posed for a shell model, provided both the membrane and flexure strain are measured.

As an example of an inverse problem that is not solvable, consider a rectangular membrane made of isotropic material, with Poisson coefficient $\nu = 0$, and subjected to a cylindrical bending with a constant deformation $\varepsilon_{11} = \mathrm{const}$ and all the other deformation components equal to zero, i.e. $\varepsilon_{22} = \varepsilon_{12} = 0$. It is trivial to verify that this problem has not a unique solution. For example, both the deformed configurations of Figure 1.3 are among the possible solutions of this problem.

At this point one could ask himself whether the inverse procedure described in this report leads to meaningful results, if any. And, indeed, the procedure fails, as it should, when applied to the ill-posed cylindrical bending problem described above. Nonetheless, it appears to work reasonably well for the test cases that were defined for this activity.
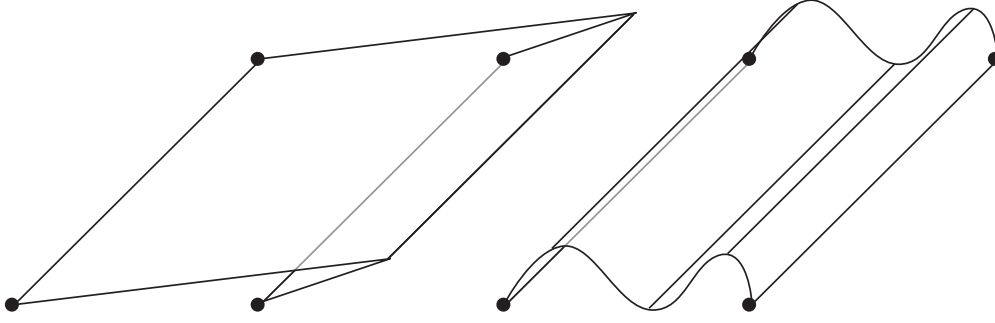
Figure 1.3: Two possible solutions for a cylindrical bending inverse problem.

An insight into this apparent paradox comes from the fact that the covariant base vectors $\mathbf{g}_\alpha$ can be used to compute the surface normal as $\mathbf{n} = \frac{\mathbf{g}_1 \times \mathbf{g}_2}{\|\mathbf{g}_1 \times \mathbf{g}_2\|}$. Then, since $\mathbf{g}_{\alpha,\beta\gamma} = \mathbf{g}_{\alpha,\gamma\beta}$, there must be some compatibility equations between the first and the second fundamental forms. These equations, known as Codazzi-Gauss equations, can be written in many ways. One of them, reported below, is

$$b_{11,2} - b_{12,1} = 0 \tag{1.22a}$$

$$b_{21,2} - b_{22,1} = 0 \tag{1.22b}$$

$$b_{11}b_{22} - b_{12}^2 = Ka \tag{1.22c}$$

where $K = \det(\mathbf{b})$ is the Gaussian curvature of the surface and $a = \det(\mathbf{a})$. Thus, what makes some problems solvable is the fact that the deformed configuration has a non-null Gaussian curvature, $K = \det(\mathbf{b}) \neq 0$, so that a link can be implicitly established between the first and the second fundamental form of the surface.

From a physical point of view, what is really important is that the deformed configuration should not allow an additional bending deformation of the surface that does not involve an additional membrane deformation as well. In other words, the problem should be membrane-dominated, in the sense defined by Chapelle and Bathe [11].

1.5 Direct Analysis

The direct analysis is performed using a tightly coupled fluid-structure co-simulation in which the structural problem is solved using the free general-purpose multibody dynamics solver MBDyn[2] [23] and the fluid problem is solved using a dedicated solver based on FEniCS [2, 3], where systems of Partial Differential Equations (PDE) and corresponding discretization and iteration strategies can be defined in terms of a few high-level Python statements which inherit the mathematical structure of the problem, and from which low level code is automatically generated. The fluid dynamics code is based on a stabilized finite element approximation of the unsteady Navier-Stokes equations (often referred to in the literature as G2 method [16]).

The multibody solver is coupled with the external fluid dynamic code by means of a general-purpose, meshless boundary interfacing approach based on Moving Least Squares with Radial Basis Function, as presented in Quaranta et al. [24]. This technique allows to compute a sufficiently regular and accurate approximation of the field of the structural displacements and velocities at the aerodynamic interface nodes, based on a set of structural nodes that is in general irregularly distributed in the neighborhood of the interface.

The membrane element, implemented in MBDyn as shown in Masarati et al. [22], is formulated as a four-node isoparametric element based on second Piola-Kirchhoff type membranal resultants. The classical Enhanced Assumed Strains (EAS) method [27] is exploited to improve the response

---

[2]http://www.mbdyn.org/.

of the element: seven additional variables for each membrane element are added to the strain vector (see for example Andelfinger and Ramm [8] for details).

The stress tensor, reorganized in form of a vector, can be expressed as a function of the strain tensor, reorganized in the same manner, using the constitutive law of the membrane element, e.g., Eq. (1.18):

$$\left\{ \begin{array}{c} \sigma_{11} \\ \sigma_{22} \\ \sigma_{12} \end{array} \right\} = \mathbf{D} \left\{ \begin{array}{c} \varepsilon_{11} \\ \varepsilon_{22} \\ \varepsilon_{12} \end{array} \right\}. \tag{1.23}$$

In case of homogeneous constitutive properties, the forces per unit span are readily obtained by multiplying the stresses by the thickness h of the membrane (otherwise, thickness-wise integration is required). Generically anisotropic constitutive properties can be defined, with matrix $\mathbf{D}$ symmetric, positive definite but otherwise arbitrarily set by the user.

Chapter 2

Results

This section presents the validation of the direct and inverse analysis by comparing the direct prediction and the reconstructed deformed shape with experimental data for prestressed rectangular membrane wings subjected to hydrostatic pressure loads (Section 2.2) and in steady level flight (Section 2.3). Since the methods described above are being evaluated for their capability of estimating an actual pressure distribution, it is first necessary to know what the applied pressure is, in order to have a basis for comparison. For this reason, two experiments were conducted in this work to provide different loading scenarios for the estimation routine.

The first scenario was a hydrostatic pressure case, where a pre-tensioned membrane was subjected to a constant known pressure. DIC measurements of strain and deformation were taken of the deformed membrane.

In the second scenario, a membrane wing was placed in a low speed wind tunnel, and wind speed and angle of attack were varied. Aerodynamic loads generated by the wing were measured, and DIC measurements of the membrane deformation were taken.

Correlation is sought with respect to experimental results obtained in test campaigns performed at Oregon State University, where elastic deformations and strains were measured using DIC [10].

Figure 2.1 summarizes the verification procedure: the strain measurements are first re-sampled onto the numerical grid that is subsequently used for IFEM analysis by means of the previously discussed MLS procedure using radial basis functions (initially developed for field interpolation at the interface between fluid and structure, see Quaranta et al. [24] for further details). The re-sampled measurements are used as inputs for the IFEM analysis. The re-sampled (transverse) displacements are used to evaluate the quality of the reconstructed displacements via IFEM and those predicted using the tightly coupled fluid-structure co-simulation.
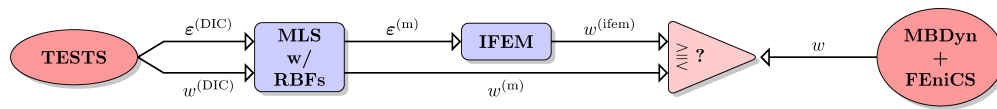

Figure 2.1: Scheme of the verification procedure.

Furthermore, total force measurements are used to evaluate the total force reconstructed by direct analysis and IFEM, and pressure distributions determined by direct analysis are used to evaluate the pressure distribution reconstructed by IFEM.

2.1 Experimental Data Re-Sampling

Measurements provided by DIC [10] include: (i) the reference location in space of an arbitrary set of points on the surface, chosen by the DIC algorithm when the measurement system is activated, (ii) the displacements of the corresponding points in the current sample, (iii) an estimate of the in-plane strains.

Data preparation, for both the measured strains used as inputs and the measured displacements used for correlation, requires re-sampling of unstructured measured fields onto the grid that is subsequently used for IFEM analysis. This is done to reduce the size of the IFEM problem, to avoid distortions in the mesh of the IFEM model, and to obtain an initial spatial filtering of the measurements.

For this purpose, a meshless mapping procedure originally developed for fluid-structure coupling is used. The mapping [24] produces a linear interpolation operator, $\mathcal{H}$, from the measurement domain, $(\cdot)_m$, to the virtual sensing domain, $(\cdot)_v$, namely $\mathbf{x}_v = \mathcal{H} \cdot \mathbf{x}_m$. Operator $\mathcal{H}$ is computed based on the initial positions of both domains; from that point on, it is used to map an arbitrary configuration of the measure domain onto the virtual sensing domain.

The participation of each component of a measure point's position to the mapping of the corresponding component of a virtual point is the same, i.e., the mapping is isotropic. As a consequence, any scalar field, as well as each component of any vector field, can be mapped separately using a subset of matrix $\mathcal{H}$, obtained for example by extracting every one out of three columns and rows of matrix $\mathcal{H}$,

$$\overline{\mathcal{H}} = \mathcal{H}(1{:}3{:}\text{end}, 1{:}3{:}\text{end}). \tag{2.1}$$

The component-by-component re-sampled strain measurements, $\boldsymbol{\varepsilon}_{i_v} = \overline{\mathcal{H}}\boldsymbol{\varepsilon}_{i_m}$, $i = 11, 22, 12$, are used as inputs for the IFEM procedure, whereas the re-sampled displacements, $\mathbf{u}_v = \mathcal{H}\mathbf{u}_m$, are used to evaluate the quality of the reconstructed displacements.

When a sufficiently large number of measurement points is required to interpolate the position of a virtual sensing point, as occurs in the present case, the procedure also produces a smoothing of the input data, acting as a spatial filter.

Thanks to the compact support used for the interpolation [24], the mapping matrix $\mathcal{H}$ is usually quite sparse: Fig. 2.2 shows the shape and fill-in (of the order of 0.05 % of non-zeroes) for the 4×8 (45 nodes), 8×16 (153 nodes) and 16×32 (561 nodes) membrane meshes mapped from 6416 DIC points. Matrix $\mathcal{H}$ can be (and it is, indeed) stored and handled exploiting such sparsity, thus drastically reducing the computational cost associated with field mapping (see Alioli et al. [4] for details).

2.2 Hydrostatic Pressure Test

2.2.1 Test Article

The experiments in Carpenter and Albertani [10] refer to a rectangular edge-clamped membrane wing, whose dimensions are $140 \times 75 \times 0.14$ mm. The wing was constructed of a pretensioned rubber latex membrane. The material properties are reported in Table 2.1. The membrane, prestrained by a 9% isotropic membrane strain ($\varepsilon_{x_0} = \varepsilon_{y_0} = 0.09$, $\gamma_{xy_0} = 0$), was subjected to hydrostatic pressure difference between the lower and the upper surface ranging from 100 Pa to 500 Pa in steps of 100 Pa.

	Tensile modulus E	Poisson's modulus ν	Density ρ
latex rubber	1.8 MPa	0.4	1350. kg/m³

Table 2.1: Membrane material properties.
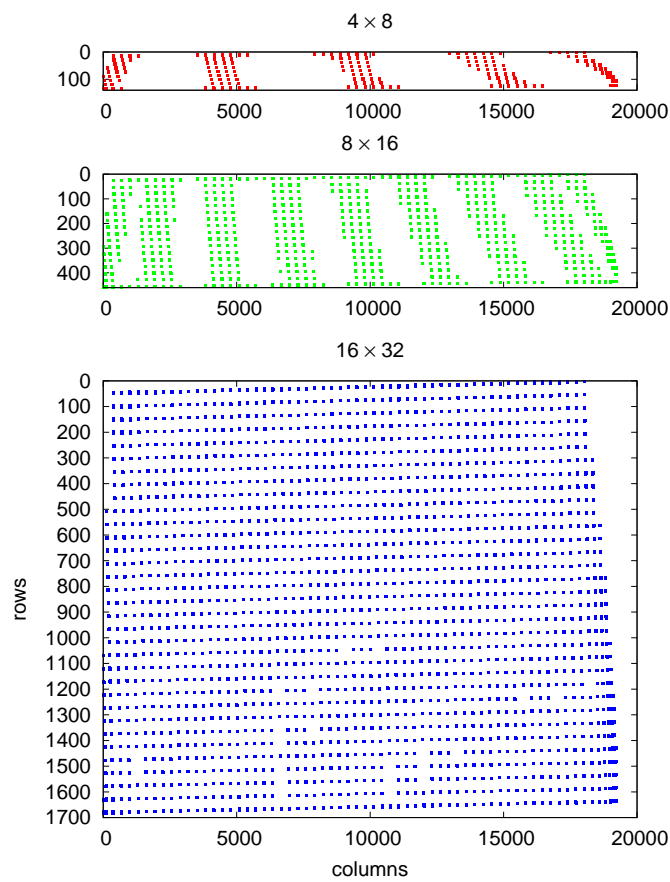
Figure 2.2: Shape and fill-in of mapping operator $\mathcal{H}$.
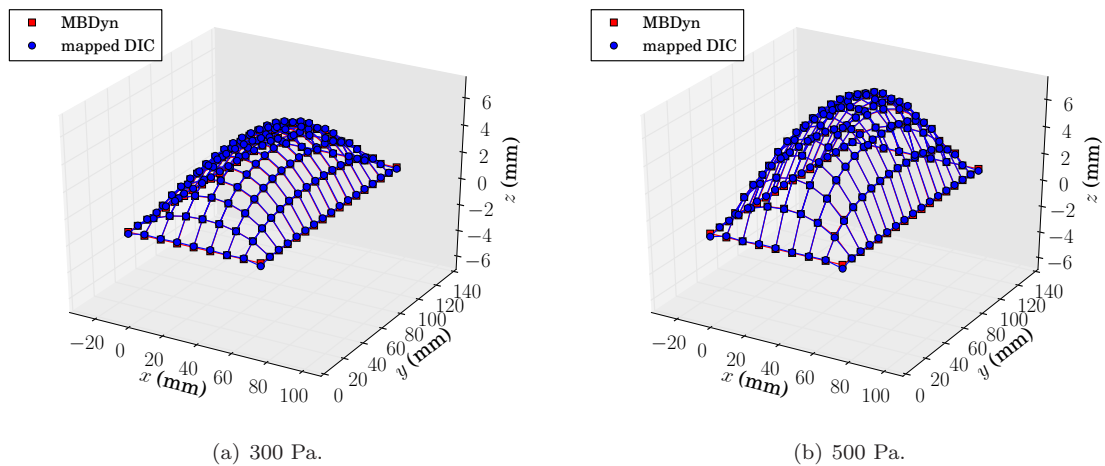
(a) 300 Pa.

(b) 500 Pa.

Figure 2.3: Numerical/experimental correlation of hydrostatic pressure problem.

2.2.2 Direct Survey

Figures 2.3(a) and 2.3(b) compare the numerical results, for the problem with 300 Pa and 500 Pa of pressure difference, with the experimental ones re-sampled on the numerical mesh using the previously discussed moving least squares (MLS) procedure. The same domain mapping algorithm is used to exchange motion and loads at the nodes between MBDyn and the fluid solver implemented in FEniCS during the coupled fluid-structure solution when the interface nodes of the structure and fluid domains do not match.

The structural grid, implemented within the multibody simulation environment provided by MBDyn, consists of 8×16 four-node membrane elements, involving 153 structural nodes (and 153 rigid body elements when a dynamic model needs to be used), as shown in Figure 2.4(a). Although not involved in the presented test cases, the mass lumped in each node is computed from the latex rubber sheet portion associated with the node, which is uniformly distributed, see Table 2.1.

A comparison of the direct solution for smaller and larger values of the prestrain is performed to study how much the problem is dependent on the value of the prestrain [4, 6]. In the experiments described in Carpenter and Albertani [10], the membrane prestrain was introduced as accurately as possible at the nominal level, but could not be checked afterwards. The facts that the numerical solutions with nominal prestrain present a very good correlation with the experiments, and that the solution is very sensitive to the amount of prestrain, indicate that the actual prestrain in the experiments was in accordance with the expected value. The inverse solution, instead, is insensitive to the amount of prestrain (matrix $\mathbf{T}$ of Eq. (1.20)) that is used to stabilize the solution process.
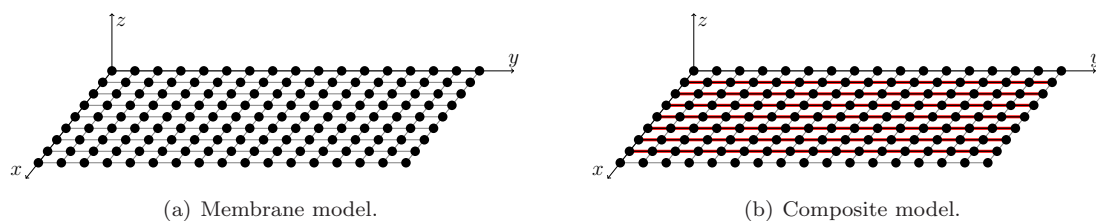

(a) Membrane model.

(b) Composite model.

Figure 2.4: Multibody membrane models.

DISTRIBUTION A. Approved for public release: distribution unlimited.

(a) 100 Pa.   (b) 200 Pa.
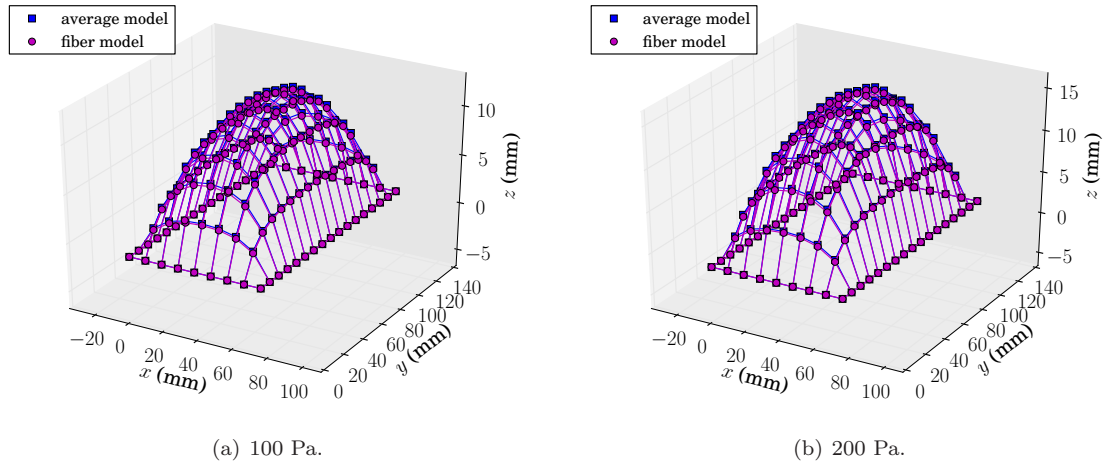
Figure 2.5: Comparison of the "fiber" and "average" model, hydrostatic pressure problem.

Non-Isotropic Membrane

A hydrostatic membrane pressure test was also conducted to characterize the behavior of a non-isotropic membrane under constant uniform pressure distribution. A study case of non-homogeneous constitutive properties of the model was investigated using the 100% fiber modulus from experimental data [32]. The membrane dimensions, loading, and boundary conditions are the same as in the direct analysis case discussed above. No prestrain was introduced herein.

A composite membrane was considered: seven fibers, which are modeled as "rod" elements, are oriented parallel to the spanwise direction (i.e., the y–axis), as shown in Figure 2.4(b). The composite is made of spandex for the fibers and silicone for the matrix. Table 2.2 presents the properties of each material. The elastic modulus at 100% strain was matched with experimental results of tensile tests [32]. The fiber diameter is equal to the thickness of the membrane.

A corresponding model of the specimen with averaged membrane/fiber properties was also investigated, by defining orthotropic constitutive properties of the membrane finite element.

	Tensile modulus E	Poisson's modulus ν
silicone matrix	0.379 MPa	0.4
spandex fiber	2.2 MPa	0.4

Table 2.2: Matrix and fiber material properties.

Figures 2.5(a) and 2.5(b) respectively compare, for the problem with 100 Pa and 200 Pa of pressure difference, the deformed shapes obtained using a model of the specimen that explicitly models the fibers (the "fiber" model) with those resulting from a corresponding model in which averaged membrane/fiber properties were used (the "average" model). As shown, the two models give consistent numerical results for hydrostatic pressure tests under controlled boundary conditions.

2.2.3 Inverse Survey

The deformed configuration of the previously investigated rectangular edge-clamped membrane is determined herein using the strain measurements derived from DIC, re-sampled onto the numerical mesh using the previously discussed MLS procedure. The membrane dimensions, loading, boundary conditions, and material properties are the same as in the direct analysis case discussed

above, see Table 2.1. A triangular mesh consisting of 8×16 elements has been used for the IFEM procedure (Figure 2.6): the strain measurements from DIC are re-mapped (and smoothed out) onto this virtual strain measurement grid, and used as inputs for the IFEM analysis.
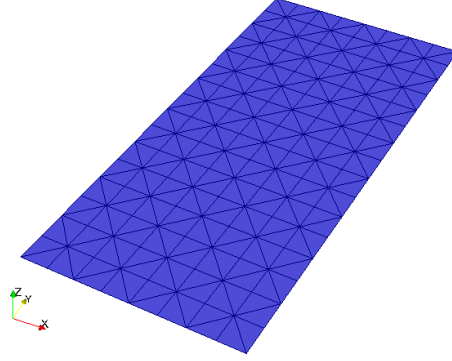

Figure 2.6: Membrane inverse analysis mesh.

In Figs. 2.7(a) and 2.7(b) the deformation shape corresponding to the inverse FEM analysis for the problems with 300 Pa and 500 Pa of pressure difference are presented, along with the experimental data re-sampled on the numerical mesh, to validate the deformations predicted by the IFEM analysis.

(a) 300 Pa.

(b) 500 Pa.
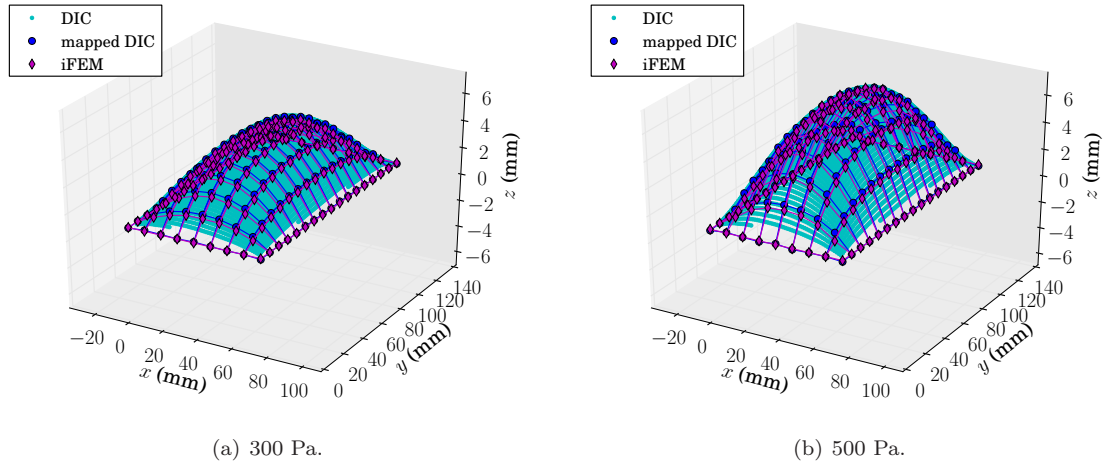
Figure 2.7: IFEM/DIC correlation of hydrostatic pressure problem.

In order to evaluate the quality of the numerical solution, a study of the sensitivity of the deformation to the refinement of the mesh used for the IFEM analysis is performed in Alioli et al. [4]. In this case, the transverse displacement error is computed as $w_{\mathrm{err}} = (w^{(\mathrm{m})} - w)/\max(w^{(\mathrm{m})})$, where $w^{(\mathrm{m})}$ is the measured transverse displacements, whereas w is the transverse displacement reconstructed via IFEM. As shown in Figure 2.8, the problem with 500 Pa of pressure difference appears to be essentially at convergence even with a mesh consisting of 8×16 elements, and the experimental displacements and those reconstructed using IFEM are in good agreement on the entire domain, including the maximum values.

The internal stresses for one particular hydrostatic pressure test at 500 Pa are shown in Figure 2.9. The stress components σ_{xx} and σ_{yy} grow from the initial value, about 0.238 MPa, to a maximum value of the order of 0.289 MPa for σ_{xx} and 0.276 MPa for σ_{yy}, respectively, in the central portion of the membrane, where the extension is maximal. The cross term σ_{xy} remains negligible.
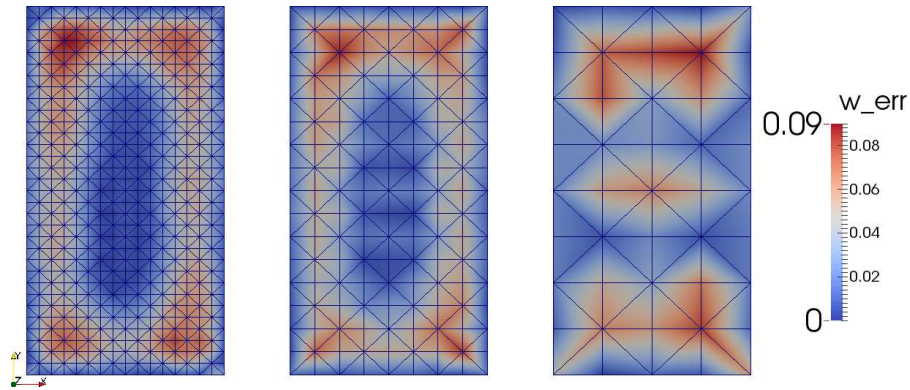
Figure 2.8: Transverse displacement error w_{err} of a rectangular membrane subjected to 500 Pa of pressure difference (left: 16×32; center: 8×16; right: 4×8).
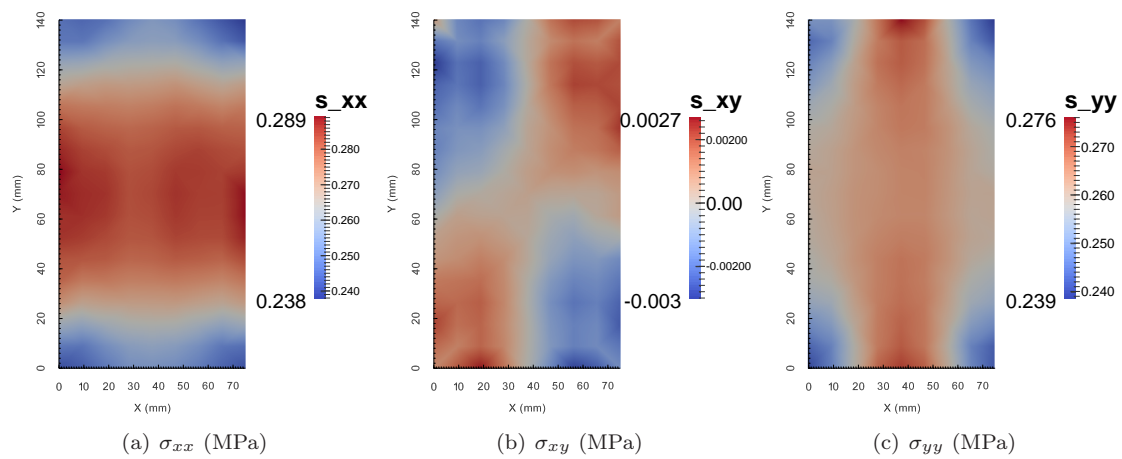

Figure 2.9: Membrane stress distribution (MPa) of a rectangular membrane subjected to 500 Pa of pressure difference.

DISTRIBUTION A. Approved for public release: distribution unlimited.

Such a change, of the order of 20%, clearly shows that the approximation of constant membrane stress, which is at the roots of linearized membrane model, is not applicable to problems of this type.

The pressure distribution for one particular hydrostatic pressure test at 300 Pa is shown in Figure 2.10, in order to compare a known input data, in this case a static pressure, with the estimated load. In fact, with a known input to the system, the output from the loads estimation procedure could be directly evaluated for its accuracy. The Figure on the left shows the ideal hydrostatic pressure applied to the membrane. The center Figure shows the pressure distribution calculated from full field DIC measurements remapped onto the numerical mesh grid as required by the IFEM procedure. The Figure on the right shows the estimated pressure distribution from the estimated displacements via IFEM analysis. The results from the hydrostatic pressure test
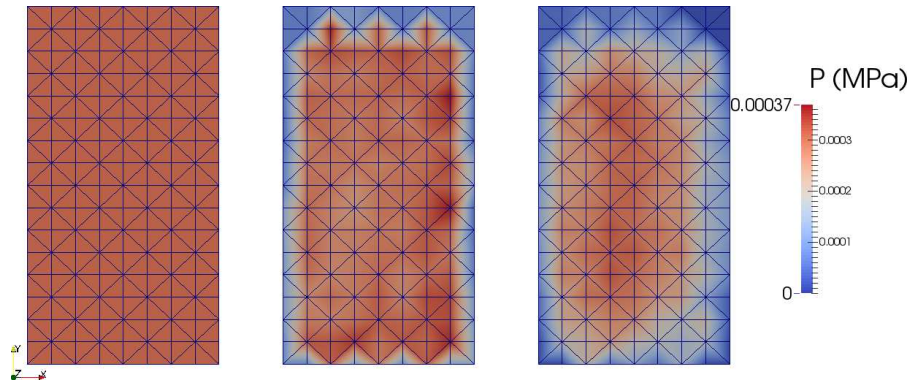
Figure 2.10: Pressure distribution (MPa) of a rectangular membrane subjected to 300 Pa of pressure difference (left: ideal pressure distribution; center: re-mapped DIC pressure distribution; right: IFEM pressure distribution).

show favorable results: the average hydrostatic pressure estimates are reasonably close to the actual applied hydrostatic load, and the error between the resultant (normal) force from the estimated pressure distributions and the one from the ideal hydrostatic pressure distribution is relatively small, as shown in Table 2.3 and in Alioli et al. [7].

Re-mapped DIC solution	0.42 %
Inverse FEM analysis	8.1 %

Table 2.3: Resultant normal force error (not considering the near-boundary region), comparison of re-mapped DIC and IFEM analysis with respect to the nominal value.

2.3   Wind Tunnel Tests

2.3.1   Test Article

The experiments conducted at OSU also involved wind tunnel tests of various 2:1 aspect ratio, rectangular, perimeter reinforced membrane wings. The membrane dimensions and the material properties are same as in Section 2.2, see Table 2.1. The wing was constructed of two shaped steel frames, sandwiching a pretensioned rubber latex membrane. The overall geometry was 140 mm $\times$ 75 mm, with a frame width and thickness of 5 mm and 1 mm respectively.

The wind tunnel, depicted in Figure 2.11(a) and 2.11(b), that was used to conduct all experiments is a low-speed wind tunnel located at Oregon State University, Corvallis (OR). The wind tunnel had a closed loop, closed test section, capable of speeds from 1 to 18 meters per second (m/s) and with a 1.3 $\times$ 1.5 m test section.

The parameters considered in these tests were AoA, initial prestrain and flow velocity. Wind tunnel tests are run for three different feasible MAV flight speeds (12, 15 and 18 m/s), at three pre-stall angles of attack (3, 6 and 9 deg), with three different initial prestrain values (2, 3.5 and 5%). The maximum Reynolds number is 67000. At each flight condition, the aerodynamic loads are measured with a six component sting balance. At the same time, the undeformed wing shape and the strain field are measured using DIC.

To evaluate the validity of the purposed approach, experimental wind tunnel loads and DIC displacements are compared to those obtained with the purposed model under varying conditions of flow velocity, AoA and initial prestrain.

(a) Overall.   (b) Zoom.
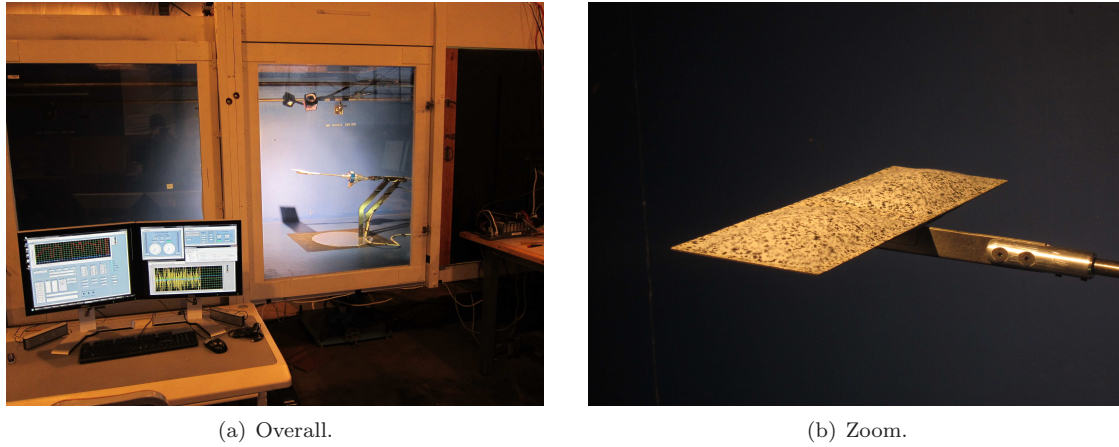
Figure 2.11: Wind Tunnel Apparatus.

2.3.2 Direct Survey

Figures from 2.12 to 2.15 compare the numerical results, with the experimental ones re-sampled on the numerical mesh using the previously discussed moving least squares (MLS) procedure. The same domain mapping algorithm is used to exchange motion and loads at the nodes between MBDyn and the fluid solver implemented in FEniCS during the coupled fluid-structure solution. The structural grid consists of 8×16 four-node membrane elements, involving 153 structural nodes, and thus 153 rigid body elements, as shown in Figure 2.4(a): the mass lumped in each node is computed from the latex rubber sheet portion associated with the node, which is uniformly distributed, see Table 2.1.
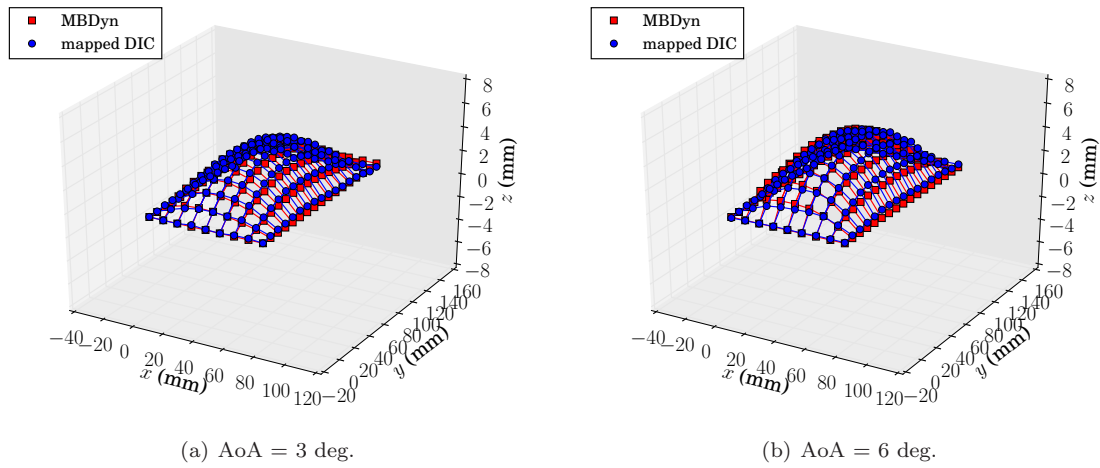
(a) AoA = 3 deg.   (b) AoA = 6 deg.

Figure 2.12: DIC/MBDyn correlation of wind tunnel tests (V = 12 m/s and PS = 2%).

(a) AoA = 3 deg.   (b) AoA = 6 deg.
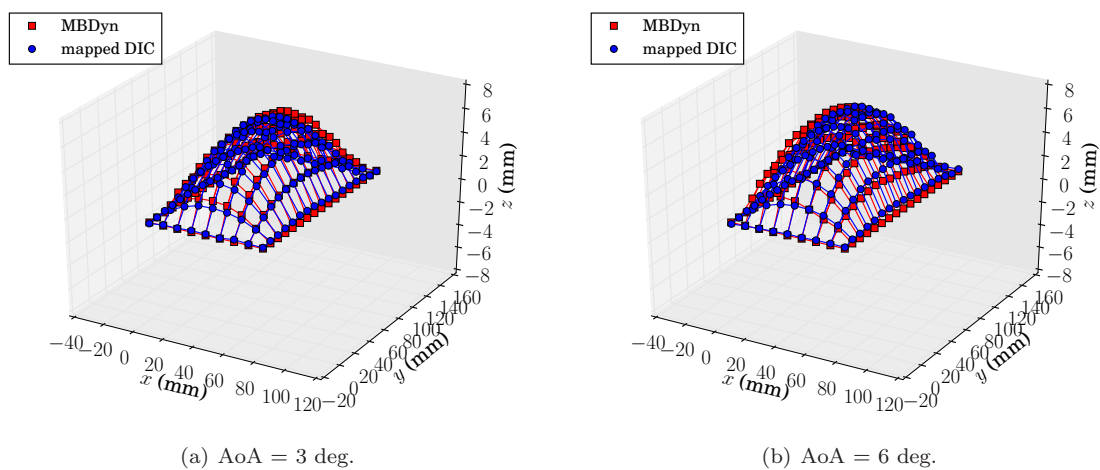
Figure 2.13: DIC/MBDyn correlation of wind tunnel tests (V = 15 m/s and PS = 2%).

DISTRIBUTION A. Approved for public release: distribution unlimited.

(a) AoA = 6 deg.   (b) AoA = 9 deg.
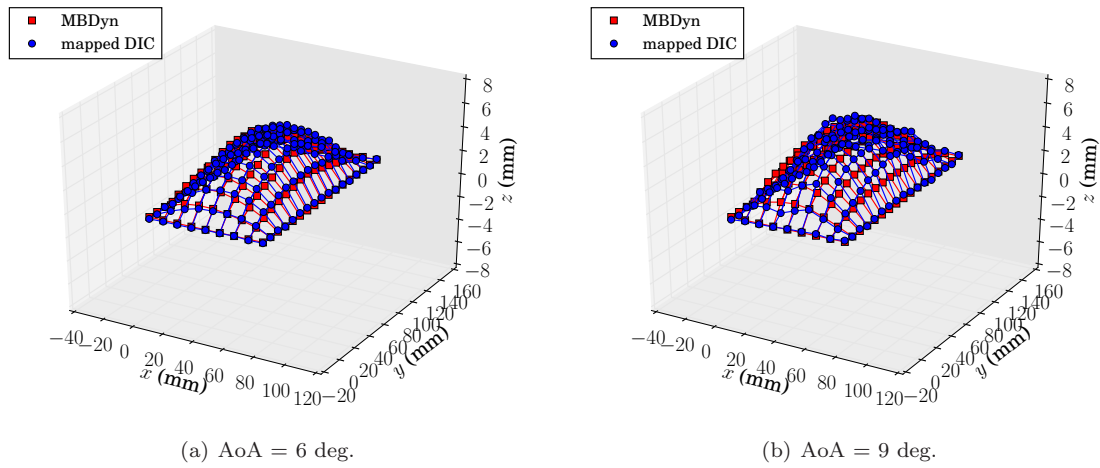
Figure 2.14: DIC/MBDyn correlation of wind tunnel tests (V = 15 m/s and PS = 5%).

(a) AoA = 6 deg.   (b) AoA = 9 deg.
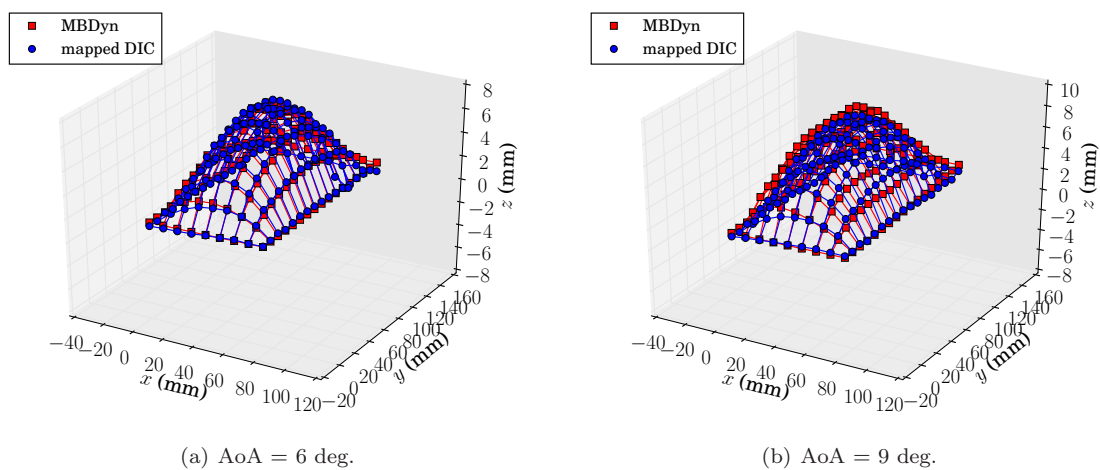
Figure 2.15: DIC/MBDyn correlation of wind tunnel tests (V = 18 m/s and PS = 5%).

2.3.3 Inverse Survey

The deformed configuration of the previously investigated rectangular membrane is determined herein using the strain measurements derived from DIC, re-sampled onto the numerical mesh using the previously discussed MLS procedure. The membrane dimensions, loading, boundary conditions, material properties are the same as in the direct analysis case discussed above, see Table 2.1. A triangular mesh consisting of 8×16 elements has been used for the IFEM procedure (Figure 2.6): the strain measurements from DIC are re-mapped (and smoothed out) onto this virtual strain measurement grid, and used as inputs for the IFEM analysis. Figures from 2.16 to 2.19 compare the deformation shape corresponding to the inverse FEM analysis with the experimental data re-sampled on the numerical mesh.

(a) AoA = 3 deg.   (b) AoA = 6 deg.
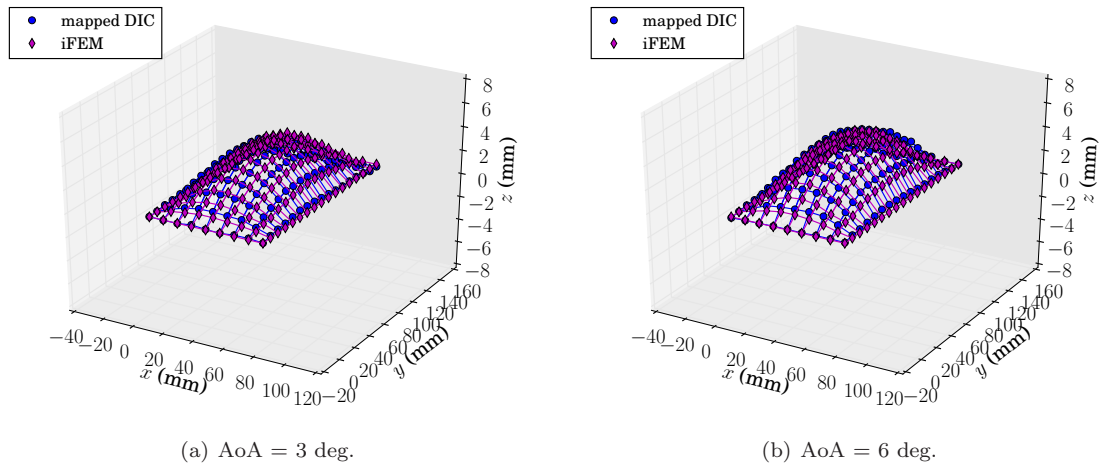
Figure 2.16: IFEM/DIC correlation of wind tunnel tests (V = 12 m/s and PS = 2%).

(a) AoA = 3 deg.   (b) AoA = 6 deg.
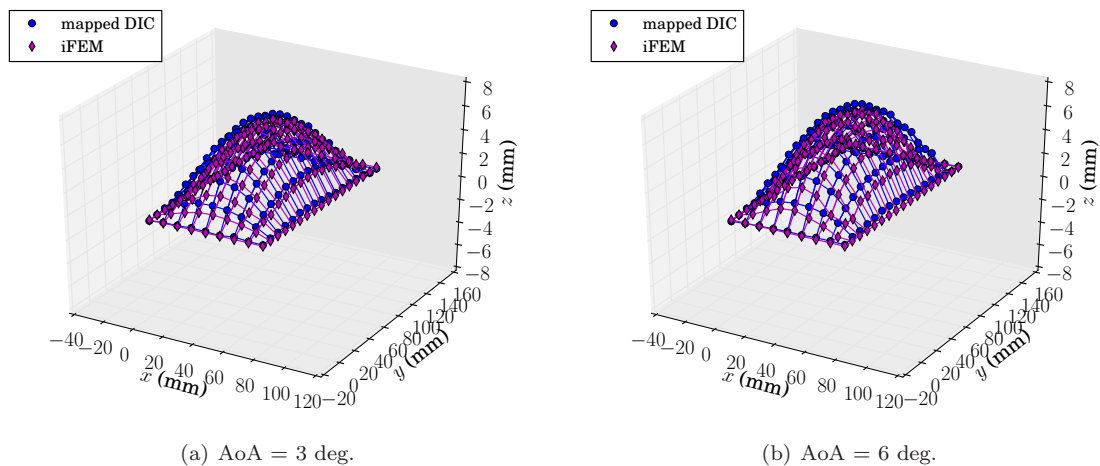
Figure 2.17: IFEM/DIC correlation of wind tunnel tests (V = 15 m/s and PS = 2%).

DISTRIBUTION A. Approved for public release: distribution unlimited.

(a) AoA = 6 deg.   (b) AoA = 9 deg.
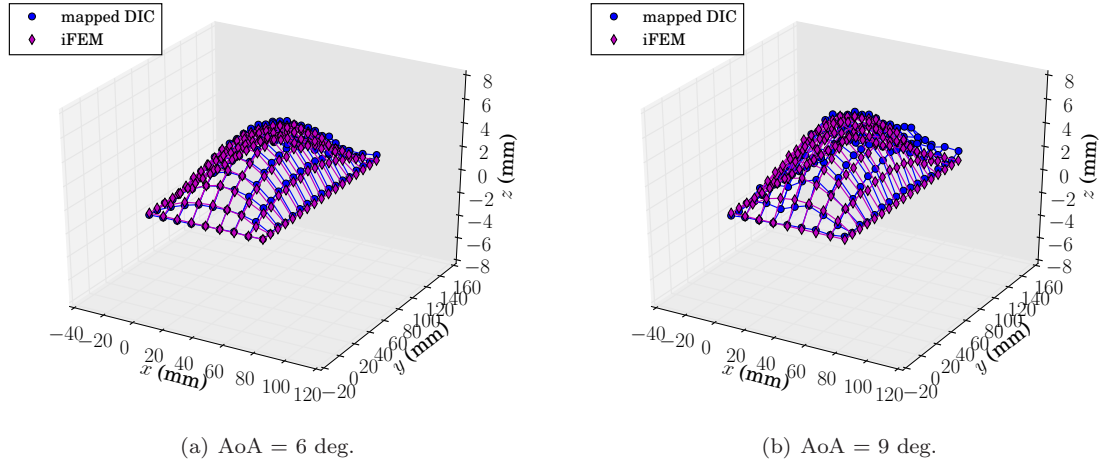
Figure 2.18: IFEM/DIC correlation of wind tunnel tests (V = 15 m/s and PS = 5%).

(a) AoA = 6 deg.   (b) AoA = 9 deg.

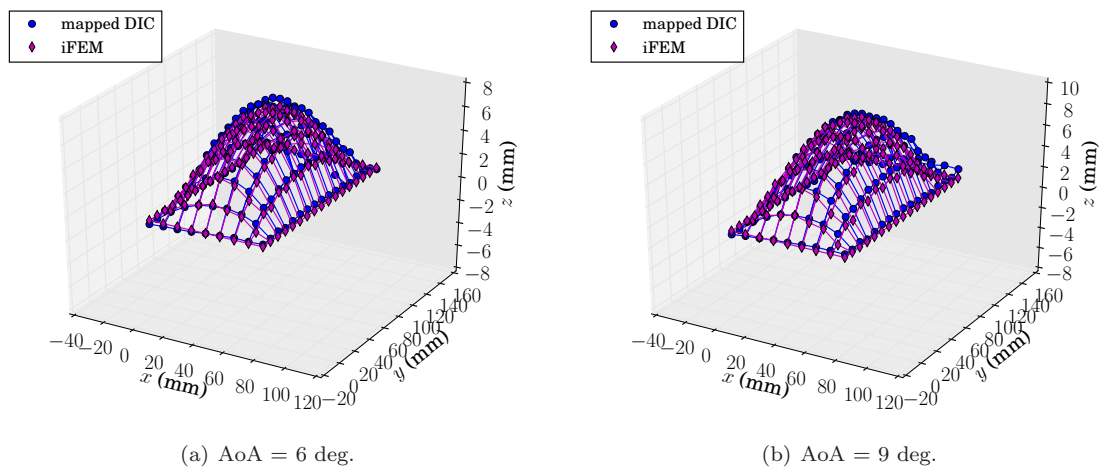**Figure 2.19:** IFEM/DIC correlation of wind tunnel tests (V = 18 m/s and PS = 5%).

Utilizing DIC data, the prediction of max camber, $\frac{z(\alpha)}{c}$, where c is the chord, can be evaluated for its accuracy and overall physical behavior. Figures 2.20 and 2.21 represent the average max (mapped) measured ("EXP") and predicted ("FSI" and "IFEM") static camber for two different values of prestrain, 2% and 5%, respectively, and for a flow velocity of $V = 12$, 15 and 18 m/s. The measured and the predicted displacement are, as expected, primarily characterized by an adaptive inflation, which increases the local camber.

(a) V = 12 m/s.   (b) V = 15 m/s.
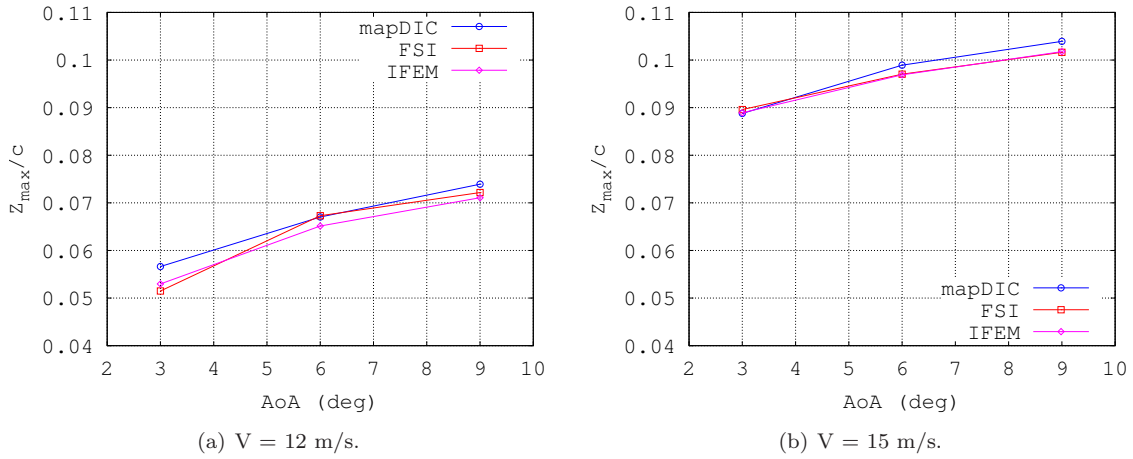
Figure 2.20: Measured max displacement from DIC data and predicted max displacement (PS = 2%).

(a) V = 15 m/s.   (b) V = 18 m/s.
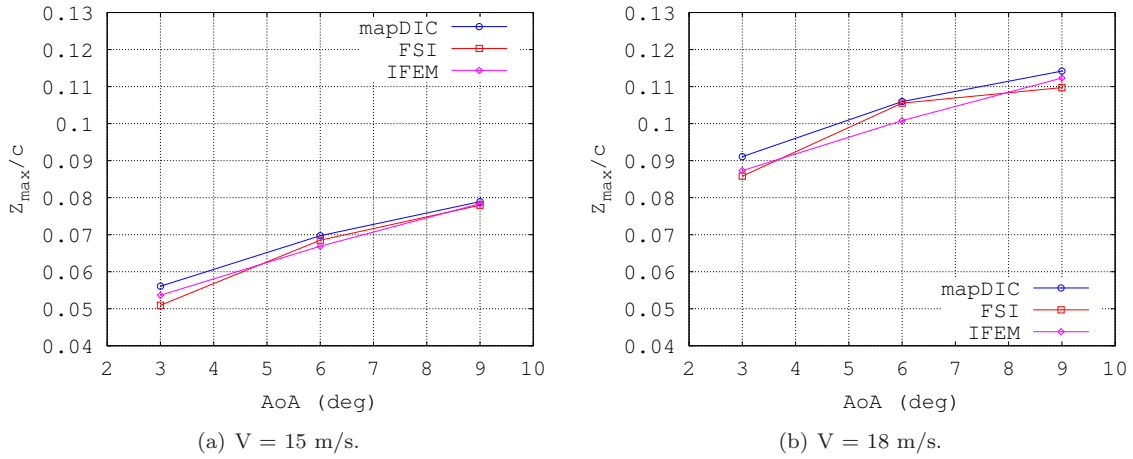
Figure 2.21: Measured max displacement from DIC data and predicted max displacement (PS = 5%).

Figures 2.22 and 2.23 show the coefficient of lift measured by the load cell attached to the wing ("EXP"). They show the coefficient of lift calculated by the coupled fluid-structure simulation ("FSI"), and also the estimated coefficients of lift found by integrating the estimated pressure distributions (calculated from the remapped full-field DIC measurements, "mapDIC," and from the estimated displacements via inverse analysis, "IFEM," respectively) to find the normal load, converting it into lift via the AoA, and finally calculating the lift coefficient.

It should be noted that those curves are nearly invariant with respect to changes in flow velocity within the range of this study (Re = 45k–67k). The error bars in the previous figures represent the standard deviations, $\sigma_{C_L^{\text{exp}}}$, which are presented for reference in Table 2.4.
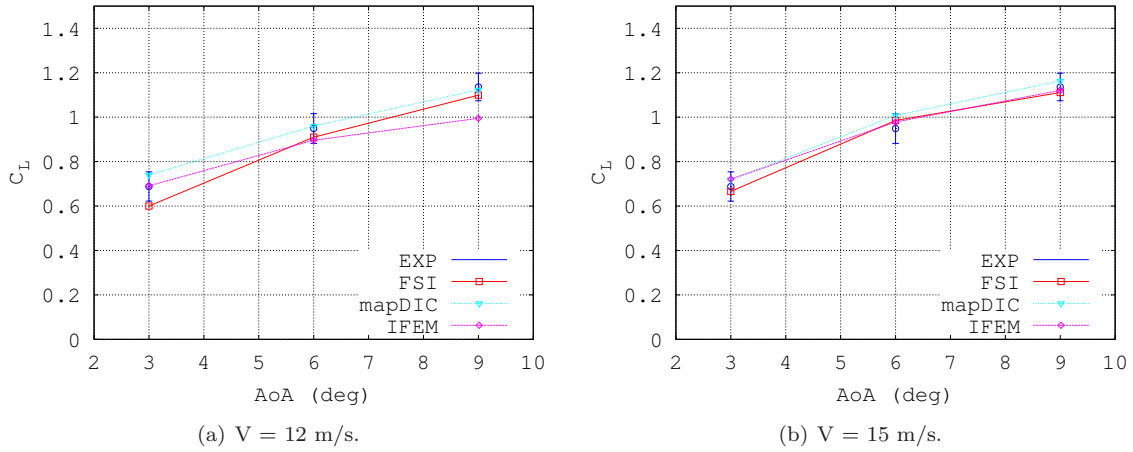

(a) V = 12 m/s.   (b) V = 15 m/s.

Figure 2.22: Static lift model and wind tunnel data (PS = 2%).

(a) V = 15 m/s.   (b) V = 18 m/s.
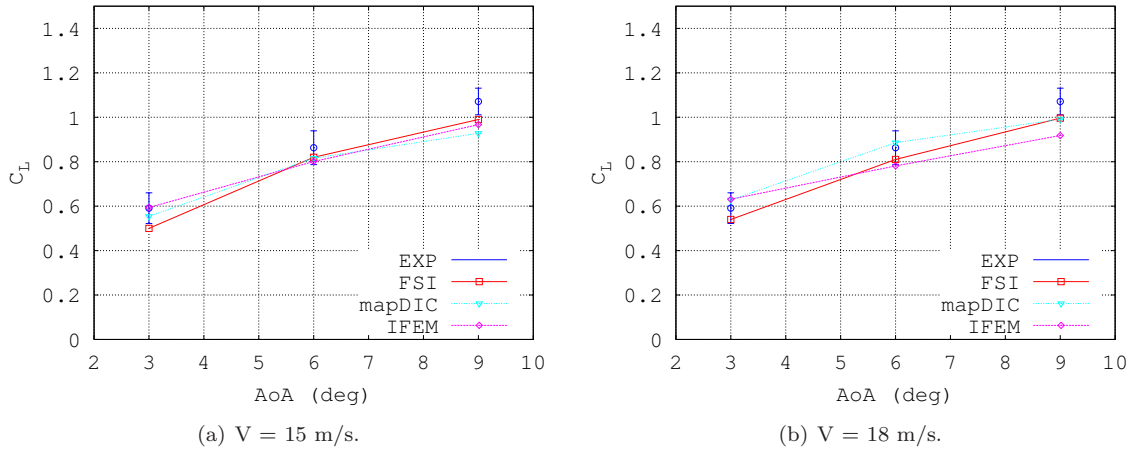
Figure 2.23: Static lift model and wind tunnel data (PS = 5%).

V(m/s)	AoA(deg)	PS (%)	C_L^{exp}	$\sigma_{C_L^{\text{exp}}}$	C_L^{fsi}	$C_{Lp^{\text{dic}}}$	$C_{Lp^{\text{ifem}}}$	w^{dic} (mm)	w^{fsi} (mm)	$\text{Err}_{w^{\text{fsi}}}$ (%)	w^{ifem} (mm)	$\text{Err}_{w^{\text{ifem}}}$ (%)
12	3	2	0.688	0.066	0.600	0.740	0.691	4.19	3.81	9.07	3.92	6.44
12	6	2	0.949	0.067	0.910	0.960	0.896	4.96	4.98	0.40	4.82	2.82
12	9	2	1.136	0.062	1.099	1.123	0.995	5.47	5.34	2.38	5.26	3.84
15	3	2	0.688	0.066	0.666	0.718	0.721	6.57	6.63	0.91	6.58	0.15
15	6	2	0.949	0.067	0.985	1.008	0.978	7.32	7.18	1.91	7.17	2.05
15	9	2	1.136	0.062	1.111	1.163	1.121	7.69	7.52	2.21	7.53	2.08
15	3	5	0.591	0.069	0.500	0.554	0.594	4.15	3.77	9.16	3.97	4.34
15	6	5	0.863	0.076	0.820	0.816	0.801	5.16	5.07	1.74	4.95	4.07
15	9	5	1.071	0.060	0.990	0.928	0.967	5.84	5.77	1.20	5.80	0.68
18	3	5	0.591	0.069	0.540	0.628	0.631	6.74	6.35	5.79	6.46	4.15
18	6	5	0.863	0.076	0.810	0.886	0.781	7.84	7.81	0.38	7.46	4.85
18	9	5	1.071	0.060	0.996	0.991	0.918	8.45	8.12	3.91	8.31	1.66

Table 2.4: Wind tunnel test, results.

Conclusions

This work presents the direct and inverse analysis of membrane elements for fluid-structure interaction problems.

To summarize: (i) a membrane inverse analysis based on a three-node membrane element was developed, based on a least squares smoothing functional that employs the complete set of strain measures; (ii) a four-node membrane element was implemented in a multibody-based co-simulation analysis for the direct simulation of coupled fluid-structure problems; (iii) the inverse analysis has been verified by reconstructing the deformed solution obtained with the analogous direct formulation applied on a different mesh and subsequently re-sampled; (iv) both the direct and the inverse analyses have been validated by comparing the direct prediction and the reconstructed deformation with experimental data for prestressed rectangular membranes subjected to hydrostatic pressure loads; (v) an approach to estimating aerodynamic load present on a flexible membrane wing from elastic strain sensor was developed.

The proposed analysis enables accurate and computationally efficient high-fidelity deformation reconstruction solutions. It is therefore applicable to both static and dynamic problems. Hydrostatic pressure tests were considered in order to compare a known input load to the estimated load. Results were favorable: the average hydrostatic pressure estimate was reasonably close to the actual applied hydrostatic pressure. In addition, the error introduced in the estimated pressure distribution can be seen in the irregularity of the estimated pressure distribution compared to the ideal pressure distribution. The proposed procedure for the reconstruction of shape and distributed loads is able to operate at sample rates of the order of 30 Hz, thus meeting the initial real-time operation requirement.

List of Figures

List of Tables

Appendix A

Inverse Analysis: 2D Example

Consider a two-dimensional problem in the x-z plane. The strain is

$$\varepsilon_x = u_{/x} + \frac{u_{/x}^2 + w_{/x}^2}{2} \cong u_{/x} + \frac{w_{/x}^2}{2}$$

where the quadratic term in $u_{/x}$ is neglected owing to the presence of the corresponding linear term. The error is $e = \varepsilon_x - \varepsilon_x^{(m)}$. The cost function becomes:

$$\begin{aligned}
\Phi &= \frac{1}{2}\left[e^2 + k\left(w_{/x} - w_{\mathrm{ref}/x}\right)^2\right] \\
&= \frac{1}{2}\left[\left(u_{/x} - \varepsilon_x^{(m)}\right)^2 + \left(u_{/x} - \varepsilon_x^{(m)}\right)w_{/x}^2 + \frac{w_{/x}^4}{4} + k\left(w_{/x} - w_{\mathrm{ref}/x}\right)^2\right]
\end{aligned} \tag{A.1}$$

Its gradient is:

$$\begin{aligned}
\Phi_{/u_{/x}} &= u_{/x} - \varepsilon_x^{(m)} + \frac{w_{/x}^2}{2} \\
&= e
\end{aligned} \tag{A.2a}$$

$$\begin{aligned}
\Phi_{/w_{/x}} &= \left(u_{/x} - \varepsilon_x^{(m)} + \frac{w_{/x}^2}{2}\right)w_{/x} + k\left(w_{/x} - w_{\mathrm{ref}/x}\right) \\
&= ew_{/x} + k\left(w_{/x} - w_{\mathrm{ref}/x}\right)
\end{aligned} \tag{A.2b}$$

Clearly $u_{/x} \equiv \varepsilon_x^{(m)}$ and $w_{/x} \equiv 0$ makes the gradient vanish when $k = 0$, although it likely is not the solution that is sought.

Consider now the Hessian matrix; its elements are

$$\Phi_{/u_{/x}u_{/x}} = 1 \tag{A.3a}$$

$$\Phi_{/u_{/x}w_{/x}} = w_{/x} \tag{A.3b}$$

$$\Phi_{/w_{/x}w_{/x}} = u_{/x} - \varepsilon_x^{(m)} + \frac{3}{2}w_{/x}^2 + k \tag{A.3c}$$

For the Hessian matrix to be positive definite, k must be:

$$k > -\left(u_{/x} - \varepsilon_x^{(m)} + \frac{w_{/x}^2}{2}\right) = -e.$$

Consider now a (simplified and heuristic) iterative solution procedure:

1. initialize $u_{/x} = 0$, $w_{/x} = 0$;

2. initialize $w_{\mathrm{ref}/x} \neq 0$ ("similar" to the expected solution);

32

3. after linearization, the increment of the derivative of the transverse displacement is

$$\Delta w_{/x} = \frac{k}{k + u_{/x} - \varepsilon_x^{(m)} + \dfrac{w_{/x}^2}{2}} \left(w_{\mathrm{ref}/x} - w_{/x} \right)$$

$$= \frac{k}{k + e} \left(w_{\mathrm{ref}/x} - w_{/x} \right) \tag{A.4}$$

which indicates that $w_{/x}$ progresses towards the reference solution with a pace that is unit when $k \to +\infty$, namely $\Delta w_{/x} = w_{\mathrm{ref}/x} - w_{/x}$; for $k \to 0$, the increase tends to vanish for positive error and, for $0 < k < -\left(u_{/x} - \varepsilon_x^{(m)} + \frac{w_{/x}^2}{2} \right) = -e$, could even be in the wrong direction (in such case, the Hessian matrix would be indefinite);

4. the increment of the in-plane displacement is

$$\Delta u_{/x} = -\frac{\left(u_{/x} - \varepsilon_x^{(m)} + \dfrac{w_{/x}^2}{2} \right)^2 + k \left[w_{/x} \left(w_{\mathrm{ref}/x} - w_{/x} \right) + u_{/x} - \varepsilon_x^{(m)} + \dfrac{w_{/x}^2}{2} \right]}{u_{/x} - \varepsilon_x^{(m)} + \dfrac{w_{/x}^2}{2} + k}$$

$$= -\frac{k \left[w_{/x} \left(w_{\mathrm{ref}/x} - w_{/x} \right) + e \right] + e^2}{k + e} \tag{A.5}$$

For $k \to +\infty$ the increment is

$$\Delta u_{/x} = -\left(w_{/x}(w_{\mathrm{ref}/x} - w_{/x}) + u_{/x} - \varepsilon_x^{(m)} + \frac{w_{/x}^2}{2} \right) = -\left(w_{/x}(w_{\mathrm{ref}/x} - w_{/x}) + e \right);$$

for $k \to 0$ it is

$$\Delta u_{/x} = -\left(u_{/x} - \varepsilon_x^{(m)} + \frac{w_{/x}^2}{2} \right) = -e.$$

The previous consideration applies about the sign of the increment.

Consider the strain $\varepsilon_x = u_{/x} + \left(\frac{u_{/x}^2 + w_{/x}^2}{2} \right)$ and equate it to its measured value, $\varepsilon_x = \varepsilon_x^{(m)}$. Assume that $w_{/x} \equiv w_{\mathrm{ref}/x}$, regardless of its value. One obtains:

$$u_{/x}^2 + 2u_{/x} - \left(2\varepsilon_x^{(m)} - w_{\mathrm{ref}/x}^2 \right) = 0 \tag{A.6}$$

whose solution is

$$u_{/x} = -1 \pm \sqrt{1 + 2\varepsilon_x^{(m)} - w_{\mathrm{ref}/x}^2} \tag{A.7}$$

and

$$u(x) = \int_0^x \left(-1 \pm \sqrt{1 + 2\varepsilon_x^{(m)}(\xi) - w_{\mathrm{ref}/x}^2(\xi)} \right) \mathrm{d}\xi \tag{A.8}$$

Nothing prevents the solution from jumping between the $\pm$ cases as needed to account for the boundary condition $u(\ell) = 0$. Note that two extreme cases could be $w_{\mathrm{ref}/x} \equiv 0$, and $w_{\mathrm{ref}/x} \equiv \pm\sqrt{2\varepsilon_x^{(m)}}$. The latter yields $u(x) = 0$.

In conclusion, a single-curvature solution cannot be reconstructed.

Bibliography

[1] J. Aernouts, I. Couckuyt, K. Crombecq, and J. J. J. Dirckx. Elastic characterization of membranes with a complex shape using point indentation measurements and inverse modelling. *International Journal of Engineering Science*, 48(6):599–611, 2010. doi:10.1016/j.ijengsci.2010.02.001.

[2] M. Alioli. Coupled fluid-structure simulation of flapping wings. Master's thesis, Politecnico di Milano, 2011. URL http://hdl.handle.net/10589/51142.

[3] M. Alioli, M. Morandini, and P. Masarati. Coupled multibody-fluid dynamics simulation of flapping wings. In *ASME IDETC/CIE*, Portland, OR, August 4–7 2013. ISBN 978-0-7918-5597-3. doi: 10.1115/DETC2013-12198. DETC2013-12198.

[4] M. Alioli, M. Morandini, P. Masarati, T. Carpenter, and R. Albertani. Nonlinear membrane direct and inverse fem analysis. In *ASME IDETC/CIE*, Buffalo, NY, August 17–20 2014. ISBN 978-0-7918-4639-1. doi: 10.1115/DETC2014-34476. DETC2014-34476.

[5] M. Alioli, M. Morandini, P. Masarati, G. L. Ghiringhelli, T. Carpenter, and R. Albertani. Nonlinear membrane inverse finite elements. In *ICNAAM*, Rhodes, GR, September 22–28 2014. doi: 10.1063/1.4912419.

[6] M. Alioli, M. Morandini, P. Masarati, T. Carpenter, and R. Albertani. Nonlinear membrane inverse finite element model for pliant wings. In *SCITECH*, Kissimmee, FL, January 5–9 2015. doi: 10.2514/6.2015-2051. AIAA2015-2051.

[7] M. Alioli, M. Morandini, P. Masarati, T. Carpenter, R. Albertani, and N. B. Osterberg. Membrane shape and transverse load reconstruction using inverse fem. In *ASME IDETC/CIE*, Boston, MA, August 2–5 2015. DETC2015-46753.

[8] U. Andelfinger and E. Ramm. EAS-elements for two-dimensional, three-dimensional, plate and shell structures and their equivalence to HR-elements. *Intl. J. Num. Meth. Engng.*, 36(8):1311–1337, 1993. doi:10.1002/nme.1620360805.

[9] A. Bakushinsky and A. Goncharsky. *Ill-posed problems: theory and applications*. Kluwer Academic Publisher, Dordrecht, Boston, London, 1994.

[10] T. J. Carpenter and R. Albertani. Aerodynamic load estimation: Pressure distribution from virtual strain sensors for a pliant membrane wing. In *54th AIAA/ASME/ASCE/AHS/ASC Structures, Structural Dynamics, and Materials Conference*, April 8-11 2013. doi:10.2514/6.2013-1917.

[11] D. Chapelle and K.-J. Bathe. *The finite element analysis of shells – fundamentals*. Springer, second edition, 2011. ISBN 978-3-642-16407-1.

[12] P. G. Ciarlet and F. Larsonneur. On the recovery of a surface with prescribed first and second fundamental forms. *Journal des Mathematiques Pures et Appliquees*, 81:167–185, 2002. ISSN 00217824. doi: 10.1016/S0021-7824(01)01236-3.

[13] M. P. Do Carmo. *Differential geometry of curves and surfaces*. Prentice-Hall, Englewood Cliffs, 1976.

[14] N. F. Foster and G. S. Dulikravich. Three-dimensional aerodynamic shape optimization using genetic and gradient search algorithms. *Journal of Spacecraft and Rockets*, 34(1):36–42, 1997. doi: 10.2514/2.3189.

[15] P. Gopalakrishnan and D. K. Tafti. Effect of wing flexibility on lift and thrust production in flapping flight. *AIAA Journal*, 48(5):865–877, May 2010. doi:10.2514/1.39957.

[16] J. Hoffman and C. Johnson. *Computational Turbulent Incompressible Flow*, volume 4 of *Applied Mathematics: Body and Soul*. Springer, 2007. doi:10.1007/978-3-540-46533-1.

[17] M. Kroon. An efficient method for material characterisation of hyperelastic anisotropic inhomogeneous membranes based on inverse finite-element analysis and an element partition strategy. *The Quarterly Journal of Mechanics and Applied Mathematics*, 63(2):201–225, 2010. doi:10.1093/qjmam/hbq004.

[18] S. K. Kyriacou, A. D. Shah, and J. D. Humphrey. Inverse finite element characterization of nonlinear hyperelastic membranes. *Journal of Applied Mechanics*, 64(2):257–262, 1997. doi:10.1115/1.2787301.

[19] K. Levenberg. A method for the solution of certain non-linear problems in least squares. *Quarterly of Applied Mathematics*, 2:164–168, 1944.

[20] Y. Lian and W. Shyy. Laminar-turbulent transition of a low reynolds number rigid or flexible airfoil. *AIAA journal*, 45(7):1501–1513, 2007. doi: 10.2514/1.25812.

[21] D. Marquardt. An algorithm for least-squares estimation of nonlinear parameters. *Journal of the Society for Industrial and Applied Mathematics*, 11(2):431–441, 1963. doi:10.1137/0111030.

[22] P. Masarati, M. Morandini, and T. Solcia. A membrane element for micro-aerial vehicle fluid-structure interaction. In P. Eberhard and P. Ziegler, editors, *2nd Joint International Conference on Multibody System Dynamics*, Stuttgart, Germany, May 29–June 1 2012.

[23] P. Masarati, M. Morandini, and P. Mantegazza. An efficient formulation for general-purpose multi-body/multiphysics analysis. *J. of Computational and Nonlinear Dynamics*, 9(4):041001, 2014. doi:10.1115/1.4025628.

[24] G. Quaranta, P. Masarati, and P. Mantegazza. A conservative mesh-free approach for fluid structure interface problems. In *Coupled Problems 2005*, Santorini, Greece, May 24–27 2005.

[25] S. Shkarayev, R. Krashantisa, and A. Tessler. An inverse interpolation method utilizing in-flight strain measurements for determining loads and structural response of aerospace vehicles. In *Proceedings of Third International Workshop on Structural Health Monitoring*, pages 336–343, 2001.

[26] W. Shyy, P. Ifju, and D. Viieru. Membrane wing-based micro air vehicles. *Applied Mechanics Reviews*, 58(4):283–301, July 2005. doi:10.1115/1.1946067.

[27] J. C. Simo and M. S. Rifai. A class of mixed assumed strain methods and the method of incompatible modes. *Intl. J. Num. Meth. Engng.*, 29(8): 1595–1638, 1990. doi:10.1002/nme.1620290802.

[28] B. Stanford, R. Albertani, and P. Ifju. Inverse methods to determine the aerodynamic forces on a membrane wing. In *48th AIAA/ASME/ASCE/AHS/ASC Structures, Structural Dynamics, and Materials Conference*, Honolulu, Hawaii, April 23–26 2007. AIAA 2007-1984.

[29] B. Stanford, M. Sytsma, R. Albertani, D. Viieru, W. Shyy, and P. Ifju. Static aeroelastic model validation of membrane micro air vehicle wings. *AIAA journal*, 45(12):2828–2837, 2007. doi: 10.2514/1. 30003.

[30] M. A. Sutton, J. L. Turner, H. A. Bruck, and T. A. Chae. Full-field representation of discretely sampled surface deformation for displacement and strain analysis. *Experimental Mechanics*, 31(2): 168–177, 1991. doi:10.1007/BF02327571.

[31] A. Tessler and J. L. Spangler. A least-squares variational method for full-field reconstruction of elastic deformations in shear-deformable plates and shells. *Comput. Meth. Appl. Mech. Engng.*, 194(2–5):327–339, 2005. ISSN 0045-7825. doi:10.1016/j.cma.2004.03.015.

[32] J. Wilcox, N. Osterberg, R. Albertani, M. Alioli, M. Morandini, and P. Masarati. Manufacturing and characterization of anisotropic membranes for micro air vehicles. In C. Ralph, M. Silberstein, P. R. Thakre, and R. Singh, editors, *Mechanics of Composite and Multi-functional Materials, Volume 7*, Conference Proceedings of the Society for Experimental Mechanics Series, pages 19–29. Springer International Publishing, Costa Mesa, CA, June 8–11 2016. ISBN 978-3-319-21761-1. doi: 10.1007/978-3-319-21762-8_3.

List of Publications

1. M. Alioli, P. Masarati, M. Morandini, T. Carpenter, N. B. Osterberg, R. Albertani, "Membrane Shape and Transverse Load Reconstruction Using Inverse FEM", submitted.

2. J. Wilcox, N. B. Osterberg, R. Albertani, M. Alioli, M. Morandini, P. Masarati, "Manufacturing and Characterization of Anisotropic Membranes for Micro Air Vehicles," Mechanics of Composite and Multi-functional Materials 7:19-29, 2016, doi:10.1007/978-3-319-21762-8_3.

3. M. Alioli, M. Morandini, P. Masarati, T. Carpenter, N. B. Osterberg, R. Albertani, "Membrane Shape and Transverse Load Reconstruction Using Inverse FEM," DETC2015-46753, ASME IDETC/CIE 2015, Boston, MA, August 2-5, 2015.

4. J. Wilcox, N. B. Osterberg, R. Albertani, M. Alioli, M. Morandini, P. Masarati, "Manufacturing and characterization of non-Isotropic membranes for Micro Air Vehicles," SEM 2015 Annual Conference and Exposition on Experimental and Applied Mechanics Hilton Orange County/Costa Mesa, Costa Mesa, CA, June 8-11, 2015.

5. Carpenter, T, Albertani, R., "Aerodynamic Load Estimation from Virtual Strain Sensors for a Pliant Membrane Wing," AIAA Journal, doi: 10.2514/1.J053291, June 2015.

6. Osterberg, B., "Experimental Investigation of Dynamic Stall on Pliant Wings for Micro Air Vehicles," FIRST PLACE graduate student paper at the AIAA Region VI Student Conference, Reno, NV, April 28-29, 2015.

7. M. Alioli, P. Masarati, M. Morandini, T. Carpenter, R. Albertani, "Nonlinear Membrane Inverse Finite Element Model For Pliant Wings," AIAA/ASME/ASCE/AHS/ASC Structures, Structural Dynamics, and Materials Conference, Kissimee, Florida, 5-9 Jan 2015, doi:10.2514/6.2015-2051.

8. M. Alioli, P. Masarati, M. Morandini, G.L. Ghiringhelli, T. Carpenter, R. Albertani, "Nonlinear Membrane Inverse Finite Elements," ICNAAM 2014, Rhodes, Greece, 22-28 September 2014, doi:10.1063/1.4912419.

9. M. Alioli, P. Masarati, M. Morandini, T. Carpenter, R. Albertani, "Nonlinear Membrane Direct and Inverse FEM Analysis," DETC2014-34476, ASME IDETC/CIE 2014, Buffalo, NY, August 17-20, 2014.

10. M. Alioli, M. Morandini, P. Masarati, "Coupled Multibody-Fluid Dynamics Simulation of Flapping Wings," DETC2013-12198, ASME 9th MSNDC, Portland, OR, USA, August 4-7, 2013